Nanostructures Studied by Atomic Force Microscopy

Ion Tracks and Nanotextured Films

BY

JUDIT KOPNICZKY

Dissertation presented at Uppsala University to be publicly examined in Häggsalen, The Ångström Laboratory, Uppsala, Thursday, November 27, 2003 at 09:30 for the degree of Doctor of Philosophy. The examination will be conducted in English.

Abstract
Kopniczky, J. 2003. Nanostructures Studied by Atomic Force Microscopy. Ion Tracks and Nanotextured Films. Acta Universitatis Upsaliensis. *Comprehensive Summaries of Uppsala Dissertations from the Faculty of Science and Technology* 905. 58 pp. Uppsala. ISBN 91-554-5795-9

The work presented in this thesis concerns two sorts of nanostructures: energetic-ion-impact-induced surface tracks and gas-deposited WO_3 nanoparticles. Our aims to characterise these nanostuctures and understand the physical principles behind their formation are of general interests for basic science as well as of the field of nanotechnology.

  AFM studies of irradiated organic surfaces showed that individual ion impacts generate craters, most often accompanied by raised plastically deformed regions. Crater sizes were measured as a function of ion stopping power and incidence angle on various surfaces. Observed crater volumes were converted into estimates of total sputtering yields, which in turn were correlated with data from collector experiments. The observations were compared to predictions of theoretical sputtering models. The observed plastic deformations above grazing-incidence-ion penetration paths agree with predictions of the pressure pulse model. However, closer to the ion track, evaporative sputtering can occur.

  AFM images of gas-deposited WO_3 nanoparticle-films indicated the formation of agglomerates. The size distribution of the agglomerates was measured to be log-normal, *i.e.* similar to the size distribution of the gas-phase nanoparticles forming the deposit. By simulations we could relatively well reproduce this observation. The agglomerates exhibited high thermal stability below 250°C when considering their size, implying that these porous films can be useful in applications involving elevated temperatures in the 250°C range. The appearance of the nanoparticles in the tapping-mode AFM images was sensitive to the free amplitude of the oscillating tip. We could show by model calculations that the high adhesion between the tip and the sample could account for some of these observations.

Keywords: ion impact, surface tracks, electronic sputtering, WO_3, nanoparticle, scanning probe microscopy, tapping mode

Judit Kopniczky, Department of Engineering Sciences, Box 534, Uppsala University, SE-751 21 Uppsala, Sweden

"The most beautiful thing is the mysterious.
It is the source of all true art and science."
/Albert Einstein/

to Vince and Bernát

List of papers

This thesis is based on the following papers, which will be referred to in the text by their Roman numerals:

I. Scanning-force-microscopy study of MeV-atomic-ion-induced surface tracks in organic crystals
    J. Kopniczky, C. T. Reimann, A. Hallén, B. U. R. Sundqvist, P. Tengvall and R. Erlandsson, *Phys. Rev. B* **49**, 625-628 (1994).

II. MeV-ion-induced defects in organic crystals
    J. Kopniczky, A. Hallén, N. Keskitalo, C. T. Reimann and B. U. R. Sundqvist, *Radiat. Meas*. **25**, 47-50 (1995).

III. Heavy-ion-induced sputtering and cratering of biomolecular surfaces
    J. Eriksson, J. Kopniczky, G. Brinkmalm, R. M. Papaléo, P. Demirev, C. T. Reimann, P. Håkansson and B. U. R. Sundqvist, *Nucl. Instrum. and Meth. in Phys. Res. B* **101**, 142-147 (1995).

IV. Damage cross sections and surface track dimensions of biomolecular surfaces bombarded by swift heavy ions
    J. Eriksson, J. Kopniczky, P. Demirev, R. M. Papaléo, G. Brinkmalm, C. T. Reimann, P. Håkansson and B. U. R. Sundqvist, *Nucl. Instrum. and Meth. in Phys. Res. B* **107**, 281-286 (1996).

V. MeV-atomic-ion-induced surface tracks in Langmuir-Blodgett films and L-valine crystals studied by scanning force microscopy
    C. T. Reimann, J. Kopniczky, E. Wistus, J. Eriksson, P. Håkansson and B. U. R. Sundqvist, *Int. J. of Mass. Spectrom. and Ion Proc.* **151**, 147-158 (1995).

VI. Track formation on LiF single crystal surface induced by high-energy Xe ions
    I.V. Vorobyova and J. Kopniczky, *Nucl. Instrum. and Meth. in Phys. Res. B* **211**, 374-382 (2003).

VII. Gas-deposited WO_3 nanoparticles studied by atomic force microscopy
    J. Kopniczky, A. Hoel, J. Kokavecz, P. Heszler and C. G. Granqvist (in manuscript).

Comments on my contribution

I was responsible for all AFM experiments and related data analysis presented in I-VII. I have actively participated in the outlining of the experiments presented in I, II, V and VII, and discussing the results. The application of L-valine single crystals for ion track studies was my idea. The collector experiments in III and IV were performed by J.E. My part in VI was the AFM work, and I participated in writing and discussing the results. The computer simulation program in VII was written by J. Kokavecz.

List of acronyms and abbreviations

AFM	Atomic Force Microscopy
LB	Langmuir-Blodgett
LHRH	Luteinizing Hormone Releasing Hormone
TOF-MS	Time-Of- Flight Mass Spectrometry
NT	Nanotechnology
NsM	Nanostructured Materials
PDMS	Plasma Desorption Mass Spectrometry
PP	Pressure Pulse
SPM	Scanning Probe Microscopy
STM	Scanning Tunneling Microscopy
TEM	Transmission Electron Microscopy
TM-AFM	Tapping Mode AFM
TS	Thermal Spike

Contents

1. Introduction

During the last few decades a new field, called nanotechnology (NT), entered the world of science and technology. The main idea behind NT is to control and/or engineer the structure and physical/chemical or biological properties of materials on the *nanometer* (atomic) *scale*. NT is quite diverse and incorporates fields ranging from molecular biology, to microelectronics [1, 2] . NT is often addressed as the technology of the future, and it is of great promise to construct highly miniaturized functional devices (*e.g.* transistors, diodes or biological sensors) [3].

The development of new methods for measuring, manipulating, and constructing objects on the nanometer scale has greatly assisted the expansion of NT. While there is a commonly held belief that NT is a futuristic science, it has already shown a number of important achievements. For example molecular-scale transistors have been realized using semiconducting carbon nanotubes [4], and it has been shown that semiconductor quantum dots are superior in high power laser diodes [5]. The potential application of hexagonal mesoporous silicas in catalysis [6] and in controlled drug release [7] has also been demonstrated. Nanoparticles are often applied as additives *e.g.* for the reinforcement of steel [8], and for the production of precipitation-hardened alloys [9].

In NT one may distinguish two major fabrication concepts: the "bottom-up", when building structures atom-by-atom, or molecule-by-molecule, and the "top-down", when carving away material from the bulk on the nanometer scale. The first branch includes various controlled deposition and self-assembly methods (that are often based on the imitation of natural biological processes [10]). The second involves all sorts of imprinting, molding or embossing methods. Lithography by photons, finely focused electron- or particle-beams and scanning probes are probably the most widely applied surface patterning methods [11].

The work presented in this thesis concerns two sorts of nanostructures: surface tracks created by energetic-ion-impact induced sputtering (a "top-down" method) and thin films constructed of tungsten-oxide (WO_3) nanoparticles by gas deposition (a "bottom-up" method).

Single-ion-impact-induced sputtering and track formation are potentially useful in the emerging fields of nanometer-scale surface tailoring technologies [12, 13]. The application of selective etching and widening of

ion-induced latent tracks for the micro/nano-machining of crystalline quartz, mica and numerous polymers has already been shown [14, 15]. MeV-atomic-ion induced surface defects can also serve as selective adsorption sites for biomolecules [16] and may form the basis of new types of biomedical sensors.

Thin films constructed of WO_3 nanoparticles are extensively applied for example as the active layer in chemical gas-sensors [17, 18], in catalytic and photocatalytic purifiers for air and water [19, 20], in photocatalytic splitting of water [21] and as the electrochromic film in "smart windows" [22, 23].

For the characterization of the nanostructures scanning probe microscopy (SPM) [24] has been applied. SPM is a well-known example of a technique which can contribute to the most important aspects of NT: imaging, modifying and manipulating matter on the nanometer-scale [25].

The motivations for the work presented in this thesis, and an outline of the experiments together with a brief introduction to SPM, are given in the following.

1.1 Ion tracks and sputtering

The understanding of ion-solid interactions is the main interest in not only some of the basic science areas, like particle physics, cosmology or geology, but also in several applied fields of science and technology. Mass spectrometry [26], microelectronics [27, 28], micro/nano engineering [12, 29-33], and cell biology [34, 35] are just a few examples where energetic-ion-impact-induced processes are utilized, and where achieving good understanding of the phenomena involved would be valuable.

Energetic ions (atomic or molecular ions with energies in the range of keV - MeV or even beyond) turn out to be suitable means for the modification of the surface or bulk structure of solids. Depending on the target material and the incoming ions' mass, nuclear charge and kinetic energy, the ions may be able to create changes only within a thin surface layer. Alternatively, ion parameters permitting, the ions may be able to penetrate far into the bulk and produce long narrow disordered zones – *bulk latent tracks* - along the ion trajectories. The intersection of a bulk latent track with the surface or vacuum interface is termed a *surface track*.

Ion tracks, on the basis of their distinct physical and chemical properties relative to the bulk material [36-38], can often be specifically processed for the fabrication of unique nanostructured products [12, 29]. By preferential chemical etching of the ion tracks, cylindrical or conical pores with diameters ranging from tens of nanometers to the micrometer size can

be obtained [39]. The pores are characterized by a large (500-1000) aspect ratio (*i.e.,* length to width ratio) and a narrow size distribution. Ion track pores in polymer films are widely applied for instance to create laboratory filtration membranes. By means of track membranes one may study cellular activities in biological systems such as transport, absorption and secretion. One-pore, oligo-pore and multi-pore membranes can serve as unique models for investigating the transport of liquids, gases, particles, solutes, electrolytes and electromagnetic waves through narrow channels [32, 33]. Track membranes can also serve as templates for the synthesis of micro- and nanomaterials, like metallic wires or tubes for small electronic devices or sensors [27, 28, 40].

Sputtering, or ejection of target material under particle-beam excitation of surfaces, is a well-known phenomenon [41] that also has a number of technological and research applications. The variety of ejected species is large. In general, photons and electrons are emitted, but most often only the ejection of atoms, molecular fragments, molecules and clusters is referred to as "sputtering".

It has been observed that energetic incident ions can be applied for the sputtering of intact, large, thermally labile organic molecules [42]. This remarkable finding has underlain the early developments in mass spectrometric investigation of peptides and proteins [43]. The most interesting question that emerged is how a fragile bio-molecule can be desorbed without fragmentation by an inherently destructive incident energetic ion. Several models have been formulated based on evaporation (*e.g.* thermal spike) and on continuum mechanical response of the excited material (*e.g.* pressure pulse, shock wave) [44-46]. However, none of these models explains all aspects of sputtering. Furthermore, even in a well-defined experimental situation, there might be a controversy over which model offers the most realistic explanation, or whether more than one mechanism might operate at the same time. This situation seems to occur when consideration is made of sputtering of organic solids by incident MeV atomic ions.

Many experiments have been performed in order to obtain a better insight into the sputtering mechanism. With mass spectrometry [47] the yield (*i.e.,* the number of secondary ions produced by one primary ion impact) as well as the angular [48] and velocity [49-51] distributions of the ejected ions were extensively studied [52, 53]. However, it has been found that the molecular ions detected by mass spectrometry represent only a tiny fraction, 10^{-4}, of the total amount of material (ions and neutrals) ejected from a bioorganic surface under fast ion impact [54]. Hence, for studies of the entire sputtering process, experiments based only on mass spectrometry (*i.e.,* the detection of ions only) are somewhat unsatisfying.

3

Also, while nearly every experiment is based on the detection and analysis of sputtered *ions,* most of the theories make predictions concerning sputtered *neutral* molecules. It has been concluded, that either theoretical models should include the ionization mechanism, or that more experiments on the neutral ejecta need to be performed [46], despite the difficulty of measuring the neutrals.

The works [I-VI] presented in this thesis concern, in various ways, the *total ejection yield* (both ions and neutrals) from organic solids bombarded by energetic ions. The introduction of atomic force microscopy (AFM) provided a new means of probing the consequences of fast-ion impact on various surfaces [I-VI]. The observed crater-like defects comprise evidence of sputtering, and material modification. The AFM study of crater size as a function of the incident ion energy loss per unit path length, *dE/dx* [II], and of the target structure [III], formed the basis for a discussion of the roles of energy density ($\propto dE/dx$) and target binding properties in sputtering and surface track formation processes. Collector experiments provided additional relative measures of the total sputtering yield and the damage cross section of organic targets [IV, V]. The dependences of these observables on the stopping power (*dE/dx*) of the primary ion were compared with model predictions [I-VI]. All the results provide evidence for highly-localized, nanometer-scale modifications of surfaces by individual ion impacts.

1.2 Nanoparticles

Nanoparticles are tiny, condensed-phase particles in the size range of ~1 - 100 nm, corresponding typically to ~50 - 5×10^7 atoms, respectively. Crystalline nanoparticles are frequently referred to as nanocrystals, while the materials constructed using nanoparticles and/or nanocrystals are often referred to as nanostructured materials (NsM). Nanoparticles are interesting from a basic perspective because of their small size. The increasing surface-to-volume ratio with decreasing size results in an increased significance of the grain boundaries (*i.e.,* surface energies) especially in the "real" nanometer range (≤ 10 nm). Thus, nanoparticles often exhibit exceptional physical properties - mostly superior - compared to the properties of bulk materials made of the same atoms. For example, high coercive force [55], giant magnetoresistance for magnetic NsM [56], high flow stress in connection with very high thermal stability, superplasticity and hardness increases [9, 57] have been observed.

4

For the fabrication and controlled deposition of nanoparticles and nanoparticle films, different techniques have been developed, such as sol-gel [58], mechanical (ball-milling) [59] and gas-phase methods [60]. By the gas-phase techniques, especially the ones based on evaporation methods, ultra-clean particles/films can be deposited [61]. During gas deposition, the nanoparticles are formed through condensation from a supersaturated vapor.

The determination of the nanoparticle or aggregate sizes is a demanding task. One of the best techniques that can be employed is transmission electron microscopy (TEM). However, in most cases TEM requires complicated and time-consuming sample preparation. Scanning electron microscopy (SEM) can also be very effective, though the achievable resolution is often not satisfactory for the imaging of small (< 10 nm) nanoparticles. Alternatively, the various SPM techniques offer high-resolution three-dimensional imaging possibilities. Nevertheless, SPM is not free from artifacts, and the interpretation of the obtained pictures is often not so straightforward. A better understanding of the operation principles is desirable.

The work presented in manuscript [VII] concerns the application of AFM for the determination of the size distribution of WO_3 nanoparticles and their aggregates in a film prepared by gas deposition. This is the way we have chosen to study the nanocluster creation and deposition processes. AFM images were found to be sensitive to the AFM operation parameters – meaning that the images are not purely topographical. Some of the observed variations could be explained by the influence of the strong tip-sample adhesion forces on the imaging process [VII].

1.3 Scanning probe microscopy

Scanning probe microscopy has revolutionized the way we look at surfaces. It provides three-dimensional real-space images of surfaces at high spatial resolution and also allows spatially localized measurements of various properties.

The history of SPM started in 1982 with the invention of the scanning tunneling microscope (STM) [62] which proved to be capable of imaging metal and semiconductor surfaces with atomic resolution. Since then a number of related probe microscopes have been developed.

The general idea behind SPM is to monitor various interactions between a small probe tip and a sample, while sweeping the tip in close proximity across the sample surface [63]. Depending on the particular SPM, the images can represent the topography, electronic structure, electric or magnetic fields, thermal gradients, or a number of other local properties of

the sample surface of interest [64, 65]. One can image hard surfaces or soft samples and operate under ambient conditions in liquids or in high vacuum. Because of this versatility, SPM techniques are extensively employed in the fields of experimental physics [66], chemistry [67], materials science [68] and biology [69, 70]. Besides "looking at" the surfaces by SPM, it is also possible to modify the surfaces on the nanometer scale [71-73]. Controlled movement of atoms or molecules may be the first step utilizing an SPM tip to build nano-machines [74, 75].

In the experiments presented in this thesis, we applied atomic force microscopy - one of the most popular members of the SPM family - in two different operation modes (continuous-contact- and tapping-mode, outlined in chapter 3) for the characterization of ion-induced surface tracks [I-V] and WO_3 nanoparticle films [VII].

# 2. Sputtering and surface modification phenomena

Ion-impact-induced sputtering of target material can generally be considered as a sequence of three steps: (I) energy loss of the primary ions in the target material; (II) conversion of the deposited energy into kinetic energy of target molecules; and (III) ejection of target molecules by breaking the intermolecular bonds. In this chapter, first the energy loss of ions in two different velocity regimes is briefly described, and then the possible energy conversion and ejection mechanisms in the high velocity regime are outlined. Since surface tracks may reveal the sputtering mechanism, surface track predictions of some of the most prominent electronic sputtering models are also summarized. Finally, a definition of damage cross section is given, which is an important parameter in total sputtering yield calculations. In all cases it will be apparent that single-ion-impact creates highly localized surface modification on the nanometer scale.

2.1 Energy loss of ions in solids

An ion that penetrates a solid or liquid loses energy mainly in collisions with target nuclei or target electrons. The ion energy loss per unit path length, dE/dx, (*i.e.,* a drag force slowing down the ion) is termed *stopping power* and depends strongly on the ion velocity (Fig. 2.1). The stopping power has two peaks, one at low primary ion velocities associated with the interaction of the incoming ion with screened nuclei of the target (nuclear stopping), and one at high velocities associated with the interaction with target electrons (electronic stopping). The two regimes in the energy loss curve are separated approximately by the Bohr velocity ($v_B = 0.22$ cm/ns, the velocity of the electron in the hydrogen atom in Bohr's semiclassical atomic model). The major variations in the energy loss mechanisms can be understood in the framework of the semi-classical atomic model according to Bohr [76].

7

For ions having a velocity much lower than the velocity of the orbiting target electrons ($v_e \approx Zv_{Bohr}/n$, where Z is the atomic number of the target and n is the principal quantum number) the energy loss will be dominated by Coulomb interactions with target nuclei screened by electrons. The energy loss in direct collisions with target electrons is small because of the large mass ratio between the interacting particles and the low energy of the incident ion. For increasing primary ion velocity, the nuclear stopping first increases because the cross section (*i.e.,* probability) for elastic collisions increases due to decreased effective adiabatic screening, and the incoming ions are more effectively slowed down. However, as the primary ion velocity further increases, the nuclear stopping decreases because the collision time (*i.e.,* interaction time) shortens.

When the velocity of the incoming ion is much higher than the velocities of the target electrons, the electrons cannot adjust their orbitals adiabatically and hence they acquire momentum in direct collisions with the incident ion. The momentum transfer from the ion to the electrons is more effective than to the nuclei due to the lower mass of the electrons. Therefore the peak of the electronic energy loss is larger in magnitude than the nuclear stopping maximum (see Fig. 2.1).
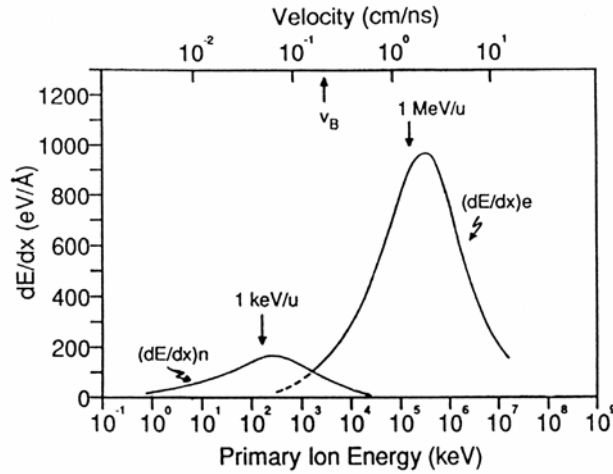
Fig. 2.1: *The nuclear and electronic stopping powers as a function of the primary ion energy (velocity). The values are for ^{127}I ion impact on the target of C_3H_5NO. The Bohr velocity, $v_B = 0.22$ cm/ns, separates approximately the velocity regimes where nuclear and electronic stopping dominate respectively.*

8

The electronic stopping power $(dE/dx)_e$ for ion-solid interactions was first derived semi-classically by Bohr [76]:

$$\left(\frac{dE}{dx}\right)_e = -\frac{Z_1^2 e^4 n_e}{4\pi \cdot m_e v^2 \varepsilon^2} \ln\left(\frac{2m_e v^2}{I}\right)$$ (1)

In this expression, e and m_e are the charge and the mass of the electron respectively, and Z_1 and v are the atomic number and the velocity of the projectile respectively. The target is characterized by the dielectric constant ε, the number density of electrons n_e and ionization potential I, that is $\propto Z_2$ i.e., the atomic number of the target. The expression indicates the main influences of v and Z_1. For the quantum theoretical derivation of $(dE/dx)_e$ the reader is referred to [77].

The primary excitation of the target *via* direct collisions between the fast incident ion and the target electrons occurs in a narrow, approximatelly cylindrical track (called the infratrack) having a radius R_i that is given by Bohr as $R_i \propto v$. Liberated electrons (secondary- or δ-electrons) emanating from the infratrack create additional electronic excitation and ionisation events in the surrounding material. The radial dimension of this outer cylindrical region (called the ultratrack) $R_u \propto v^2$ is determined by the range of the most energetic electrons released from the infra track [26, 78].

Different primary ions having the same velocity produce secondary electrons of the same maximum energy and therefore tracks of the same diameter, independent of the ion atomic number [79]. However, the *energy density* inside the track increases with the atomic number of the impacting ion, since $(dE/dx)_e \propto Z_1^2$ (see Eqn. 1).

Nuclear and electronic stopping, both entailing a degree of energy deposition at and near a surface, leads to ejection of material from the target. This phenomenon is called *nuclear sputtering* [80] or *electronic sputtering* [81, 82], depending on the nature of the energy deposition.

In the experiments presented in this thesis the energy of the primary ions fell in the MeV range where electronic sputtering was the dominating process. In the following, only electronic sputtering is discussed in more detail.

2.2 Conversion of electronic excitations into atomic motion

Electronic sputtering is a complex phenomenon, since it involves the conversion of the "motionless" electronic (potential) energy into atomic motion (kinetic energy). Also, the amount of energy deposited can be quite high, and unique physico-chemical material responses may come into play.
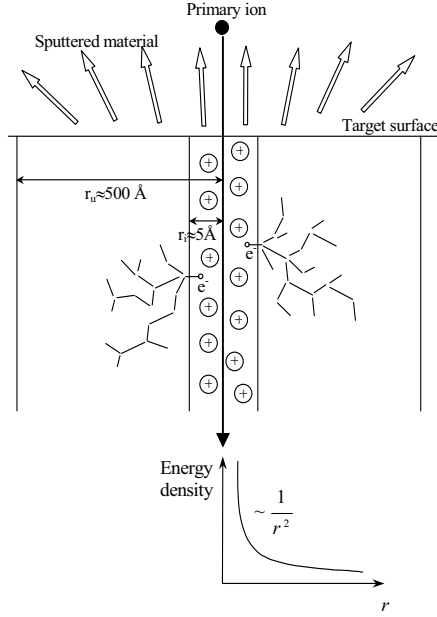
When an energetic ion passes through a target, it deposits energy electronically according to the electronic stopping power, $(dE/dx)_e$ (Eqn. 1).

It is believed [83] that the electronic excitations and ionizations must survive for a sufficiently long time ($\sim 10^{-13}$ s), in order for their energy to be converted into kinetic energy of atomic and molecular motion. Therefore conducting solids, in which the electrons can swiftly repopulate ionized atoms and/or dissipate their energy at long distances *via* the conduction band, would display little atomic displacement in response to a fast ion impact. However, at high $(dE/dx)_e$ even conductors can display tracks after ion bombardment [84].

Fleicher *et al.*[83] proposed that latent tracks observed in insulators are formed as a consequence of electron depletion. The repulsive Coulomb force in the evolved positively charged track near the ion path causes atomic motion and track expansion. This mechanism is referred to as a Coulomb explosion [83]. It is, however, uncertain whether the conductivity in the highly ionized region is low enough to provide a sufficient lifetime for the positively charged track for significant atomic displacement to occur [85]. There have been several other mechanisms proposed as well for the energy conversion into atomic motion. Electronic excitation of chemical bonds to long-lived repulsive states and subsequent separation of the molecules [85], or vibrational excitations of chemical bonds leading to larger separation between the atoms - due to the anharmonicity of the interatomic potential - are two examples [45, 86]. A schematic drawing of the initial events occurring in the target during electronic sputtering is shown in Fig. 2.2.

2.3 Ejection of material from the surface

A complete description of electronic sputtering would require the solution of the time-dependent Schrödinger equation for a large number of interacting particles. For a simpler analytical description of the ejection process, a continuum mechanical model of the energy (and momentum) flow in the material with an ejection criterion can be used [87]. This will be briefly outlined in the following.

Primary ion

Sputtered material

Target surface

$r_u \approx 500$ Å

$r_i \approx 5$Å

e⁻

e⁻

Energy density

$\sim \dfrac{1}{r^2}$

r

Fig. 2.2: *Illustration of the initial stages of energy deposition occurring during electronic sputtering. About half of the total amount of the electronically deposited energy of the incident fast ion causes primary excitations and ionizations close to the ion path (infra track). The other half of the energy is deposited in a surrounding region (ultra track) by the secondary electrons (δ-electrons) emanating from the infra track and causing further ionizations and excitations. The energy density falls off as $1/r^2$ radially outwards from the track center[52].*

An ion traversing a solid is assumed to deposit kinetic energy ΔE_i in a small spherical volume of radius r_0. If nearly every particle in the energized region acquires significant kinetic energy, then the energized region is referred to as a "spike".

In *diffusive spike* models it is assumed that the energy propagates according to a simple diffusion equation [87]:

$$\nabla\left[\kappa\nabla\varepsilon(r,t)\right] = \frac{\partial\varepsilon(r,t)}{\partial t} - \frac{\varepsilon}{\tau} \tag{2}$$

In this equation, κ is the diffusivity, $\varepsilon(r,t)$ is the volume energy density as a function of spatial coordinates and time, r is the perpendicular distance from the incident ion track and τ is the time constant related to energy dissipation. The energy density in the solid at a location r at a time t is obtained by solving the diffusion equation for spherical sources along a semi-infinite track with cylindrical symmetry and coordinates, resulting in:

$$\varepsilon(r,t) = \frac{\Delta E_i}{\pi^{3/2}(r_0^2 + 4\kappa t)^{3/2}}\exp\left(-\frac{r^2}{r_0^2 + 4\kappa t}\right)\exp\left(-\frac{t}{\tau}\right) \tag{3}$$

11

Evaporative or *thermal spike* (TS) models describe sputtering by the thermally activated flux of particles evaporating from the surface [88-90]. Typically, an Arrhenius-type flux $\Phi \propto \exp(-U_M / kT(r,t))$ can be postulated [89] where U_M is the molecular surface binding energy. $T(r,t)$, the local temperature, can be identified with $\varepsilon(r,t) / k \cdot n_M$ where n_M is the number density of molecules. A general expression for the evaporative desorption yield, Y, due to a thermal spike is written as a surface integral:

$$Y_{TS} = \int_0^\infty dt \int_0^\infty 2r\pi dr \Phi[T(r,t)] \tag{4}$$

A central result of the cylindrical thermal evaporation model when a narrow initially energized region is assumed is that the scaling of Y with $(dE/dx)_e$ is [88]:

$$Y_{TS} \propto (dE/dx)_e^2 \tag{5}$$

What is typically neglected in the thermal spike model is that the energy density exhibits a *gradient* radially from the ion track and outwards to the surface as well. The consideration of this *energy density gradient* leads to another approach of the sputtering mechanism, discussed below.

According to the *pressure pulse* (PP) model [87] sputtering is determined by the *energy density gradient:* $-\nabla\varepsilon(r,t)$, which can be considered as a net force per unit volume on a region of material containing energy density $\varepsilon(r,t)$. The temporally transient nature of the solution for $\varepsilon(r,t)$ means that $-\nabla\varepsilon(r,t)$ is closely related to a sort of "pressure pulse". The momentum acquired by a molecule experiencing the pressure pulse is:

$$p(r) = \frac{\beta}{n_M} \int_0^\infty [-\nabla\varepsilon(r,t)] dt \tag{6}$$

Here β is a thermodynamical proportionality constant describing the fraction of the energy in the solid which appears as translational kinetic energy rather than as internal energy of molecules. Desorption occurs when a molecule acquires a critical normal momentum $p_\perp \geq p_c = (2MU_M)^{1/2}$, where M is the molecular mass and U_M is the molecular binding energy. For the scaling of the sputtering yield with $(dE/dx)_e$, the pressure pulse model predicts that:

$$Y_{PP} \propto (dE/dx)_e^3 \tag{7}$$

In the alternative *shock wave* model [91, 92] the high energy density in the track results in the formation of a shock wave, that is spread in the solid according to a *wave equation*. In its consequences, (*i.e.* Eq. 7 holds) the shock wave model resembles quite closely the pressure pulse model.

2.4 Surface tracks: a long-term manifestation of sputtering

Surface tracks can easily be the subject of various surface imaging techniques (*e.g.* AFM, SEM) [I-VI]. The question is, wheter the surface tracks can be considered as "fingerprints" of the sputtering process. What sort of surface tracks do the above discussed sputtering models predict?

The *pressure pulse* and *shock wave* models [81, 87] as well as molecular dynamics simulations [50, 93, 94] of the sputtering process predict hemispherical crater formation for *normal incident* ions. The crater radius can be expressed as [87]:

$$r_{c,PP} = \frac{1}{p_c} \cdot \left(\frac{dE}{dx} \right)_{eff} \cdot \frac{\beta}{4\pi\kappa} \cdot V_M \propto \frac{M_W}{U_M \cdot V_M^{1/3}}$$

(8)

where $p_c = \sqrt{2M_W U_M}$ is the critical normal momentum needed for one molecule to be ejected, M_W is the molecular weight and U_M is the molecular binding (sublimation) energy of the target, $(dE/dx)_{eff} \approx 0.01(dE/dx)_e$ [44] is the effective electronic stopping power contributing to the pressure pulse , V_M is the volume occupied by one molecule, β is a the thermodymanical constant as in Eqn. 6 (of the order of 2/3), and $\kappa \propto \sqrt{2U_M / M_W} \cdot V_M^{1/3}$ is the "collisional" thermal diffusivity [87].

For *grazing incident* ions the maximum crater width (*W*) perpendicular to the ion path is independent of the angle of incidence; the length (*L*) of the crater along the surface azimuth of the ion track is simply $W \cdot \{\cos(\theta)\}^{-1}$, where θ is the ion angle-of-incidence with respect to the surface normal [95].

The *thermal spike* model also predicts the formation of surface craters. For normal incident ions a simple expression has been given [89]:

$$r_{c,TS} = \sqrt{\frac{k}{\pi} \cdot \frac{(dE/dx)_{eff}}{C \cdot U_M}} \propto \sqrt{\frac{M_W}{U_M}}$$

(9)

Here k is Boltzmann's constant; C is the heat capacity per unit volume, taken to be $C = 3k/2V_M$, so that the molecules are regarded as being structureless point particles. However, if the internal molecular modes participate in the energy diffusion as well (*i.e.,* if the thermal spike is in thermal equilibrium), then the expression for C above should be multiplied by the number of atoms per molecule, N.

In the work presented in this thesis we discuss our experimental results in the framework of the various sputtering models through their different predictions for the sputtering yield (compare Eqns. 5 and 7) and crater radius (compare Eqns. 8 and 9) as a function of $(dE/dx)_e$.

However, by measuring the kinetic energy and angular distribution of the ejected species, one could obtain a deeper insight into the sputtering mechanism [53]. The *thermal spike* model assumes that the molecules are evaporated in a *symmetric* cosine polar-angular distribution [96]. *Pressure pulse or shock wave* models both assume that a transient energy density gradient results in impulsive transfer of momentum to the molecules. Since the momentum transfer to some location in the target depends on the excitation geometry, the PP/SW models predict a *correlation* between the ion incidence angle and the angular distribution of sputtered material. The predicted angular distribution is sharply peaked *away* from the direction of the incident ion [50, 87, 92, 95, 97].

2.5 Damage cross section

The energy loss per unit path length, *dE/dx*, of *e.g.* a 1.1 cm/ns (0.6 MeV/u) ^{127}I ion incident on an organic target is ≈ 8 keV/nm [98]. The region directly excited by the incident ion, the infratrack, is characterized by a radius $R_i \approx 0.5$ nm [78]. The region which is excited and ionized by released target electrons spreading out from the infratrack, the ultratrack, is characterised by a radius $R_u \approx 40$ nm [99]. The energy density in the infratrack, ≈ 10 keV/nm^3, is sufficient to break all inter- and intra-molecular bonds in the region. The resulting energy density $\approx 10^{-15}$ s after the ion passage is approximatelly described by $\varepsilon(r) \propto r^{-2}$ [99]. Thus the energy density at $r = 5$ nm is ≈ 100 eV/nm^3, still enough to break at least hydrogen bonds. Because energetic secondary electrons leave the infratrack and cause additional modifications in the surrounding target material, the radius $r = 5$ nm can be considered to be a lower limit on the size of the region which is completely damaged by the incident ion. Since also fluctuations are involved in the energy loss events, the region where damage can occur around the ion track core does not have sharp boundaries. It is important to

emphasize that by the word *damage*, we mean all types of physical and chemical changes induced by the incident ion.

A quantity, called *damage cross section*, σ, is introduced in order to quantify the effective damaged zone around the path of the impacting ion.

If one monitors the sputtering yield (Y) of *intact* molecules/molecular ions with increasing primary ion fluence ϕ (*i.e.,* the number of incident ions per unit area) an exponential decrease of Y can be observed:

$$Y(\phi) = Y_0 e^{-\sigma \cdot \phi}, \tag{10}$$

where Y_0 is the yield of intact molecules sputtered from an undamaged target spot. Since this drop of Y with increasing primary ion fluence is related to the increasing area of damaged regions, the quantity σ is termed *damage cross section*. In this measurement σ is basically a "signal reduction cross section" due to damage. Damage cross section is another measure of how localized the effect of an ion is.

The damage cross section has been measured for various amino acids and peptides for primary ions with different *dE/dx* [IV] [100, 101]. Alternatively, irradiation-induced reduction of molecule-specific optical absorbance [51] and the enhancement in the number of paramagnetic centers, as measured by electron paramagnetic resonance [102], have also been used to determine damage cross sections.

The modified physical/chemical properties of the damaged region may have several nanotechnological applications. Preferential chemical etching of the damaged zone (*i.e.,* ion track etching) has already been discussed in the introduction. Since the damage induced depends on the material properties of the target as well, damage could also be a means to probe these material properties on the nanometer scale [103]. Focused ion beam nanolithography and ion-implantation, two additional technological examples where target material is modified by energetic ions, are frequently applied in the field of microelectronics [104]. Another area, still under active development as well as application, is controlled cell inactivation in cancer therapy [35].

3. Atomic force microscopy

A large number of SPM variants have been developed based on the detection of *forces* between the probe tip and a sample.

A variety of tip-surface interactions may be measured by an atomic force microscope (AFM), depending on the separation between tip and sample. At short distances the tip predominantly experiences interatomic forces: the very short range (≈ 0.1 nm) Born repulsive forces and the longer range (up to 10 nm) van der Waals forces. Further away from the surface where the van der Waals forces decay rapidly and become negligible (100-500 nm above the surface), long-range electric, magnetic and capillary forces are still significant and can be probed. The operation modes applied in the work reported in this thesis mainly involve short-range interatomic forces, and these will be briefly described.

At distances of a few nanometers, van der Waals (VdW) forces are sufficiently strong to move macroscopic objects, such as AFM cantilevers (to which the scanning tip is attached). VdW forces are usually attractive and rapidly increase as atoms/molecules approach one another. VdW interactions consist of three components: polarization, induction and dispersion forces. For two identical interacting gas molecules, for example, the VdW potential (U_{vdW}) can be expressed as the sum of these three components as:

$$U_{vdW} = -\left(\frac{1}{4\pi\varepsilon_0}\right)^2 \left(\frac{\mu^4}{3kT} + 2\mu^2\alpha + \frac{3}{4}\alpha^2\hbar\omega\right)\cdot\frac{1}{z^6} \approx -\frac{C_1}{z^6} \qquad (11)$$

where ε_0 is the permittivity of vacuum, T is the temperature, μ is the permanent dipole moment and α is the polarizability of the molecules. $\hbar\omega$ is the ground state energy of electrons, z is the distance between the interacting molecules, and C_1 is a constant, known as the London coefficient. Dispersion forces (London forces) generally dominate over orientation and induction forces (except in the case of strongly polar molecules). Since dispersion forces originate from the instantaneous fluctuations of electrons around the nuclei, they act between all materials. (Such forces are also called instantaneous-dipole - induced-dipole forces.)

If the probe further approaches the sample and the electronic wavefunctions of the outermost probe atoms and sample atoms start to overlap, strong repulsive forces arise. These forces, also called Born repulsive forces, are characterized by having very short range and increasing very sharply as two molecules come together. The repulsive potential is most often expressed as a power-law potential:

$$U_{rep.} = \frac{C_2}{z^{12}} \qquad (12)$$

The total intermolecular pair potential is obtained by summing the attractive (Eqn. 11) and repulsive (Eqn. 12) potentials. The expression is the well-known Lennard-Jones potential:

$$U = \frac{C_2}{z^{12}} - \frac{C_1}{z^6} \qquad (13)$$

where C_1 and C_2 are the corresponding coefficients for the attractive and repulsive interactions.

Describing the AFM tip and sample interactions, the attractive and repulsive potential pairs have to be summed for all interacting atoms with consideration of the local geometry, material properties, and the non-additive characteristics of the VdW interactions [105]. In practice, an experimental force *vs.* distance curve is applied, that can be registered by AFM while approaching the tip towards the sample. Typical variation of the tip-sample interaction force with the separation in between them is shown in Fig. 3.1.

The VdW potential between two *macroscopic* bodies, for example a sphere (like the AFM tip end) and a plane (the sample surface), can be approximated as [105]:

$$U_{VdW} = -\left(\frac{AR}{6z} \right), \qquad (14)$$

and the VdW force as:

$$F_{VdW} = -\frac{dU_{VdW}}{dz} = -\frac{AR}{6z^2}, \qquad (15)$$

where R is the radius of the sphere and A is the Hamaker constant, $A \approx \pi^2 C_1 \rho_1 \rho_2$, that characterizes the properties of the interacting materials

(and was more precisely given by Lifshitz [105]). C_1 is the London coefficient and ρ_1 and ρ_2 are the densities of the interacting bodies.

A model concerning *repulsive forces* between *macroscopic* objects, was formulated by Hertz more than hundred years ago. According to him, the indentation force acting when a sphere is pressed into a flat surface can be given as [24]:

$$F_{ind.} = \sqrt{K^2 R d^3} \, ,$$ (16)

where K is the effective elastic modulus ($\propto$ Young's moduli and Poisson coefficients of the tip and the sample); d is the indentation depth. However, since Hertzian mechanics assumes that there is no adhesion or surface forces (*i.e.*, no attraction whatsoever), it is not the best model for describing a typical AFM experiment [106]. Alternative continuum mechanical models that include surface forces are summarized in [106].

Operation modes in AFM can be discussed in terms of the applied force regimes (contact, non-contact and intermittent-contact, see Fig. 3.1) or in terms of the force sensing technique employed (deflection or quasistatic (dc) mode and vibrational or dynamic (ac) mode) [24]. The operating modes of AFM will now be discussed in more depth theoretically.
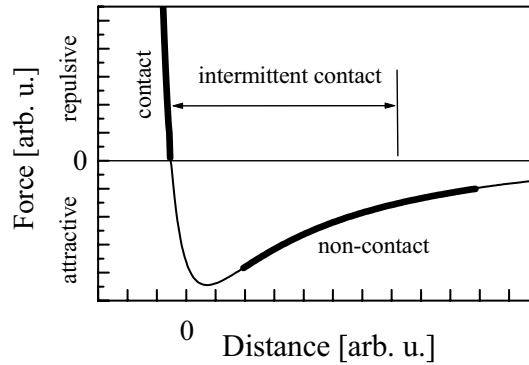
Fig. 3.1: Empirical force vs. distance (i.e. tip-sample separation) curve that reflects the main interactions between the scanning tip and sample surface during AFM measurements. Various AFM mode regimes are indicated. (Experimental force-distance curves, taken by AFM usually represent a full approach-retract cycle, and often exhibit a hysteresis, reflecting on the adhesion forces and eventual capillary forces as well. For simplicity, these forces are disregarded here.)

18

3.1 Force detection and AFM imaging

The underlying principle of AFM is that the interactions between the sample and the end of a probe tip, that is mounted on a cantilever, result in a response in the cantilever, notably a deflection.

3.1.1 Continuous contact mode AFM

In continuous *contact mode* [63], also known as *repulsive mode*, an AFM tip makes soft "physical contact" with the sample (see Fig. 3.1). The sharp probe tip, often a pyramidal-shaped etched silicon nitride tip, is attached to the end of a V-shaped spring cantilever with a low spring constant, typically between 0.06 N/m and 0.6 N/m. As the scanner gently traces the tip across the sample, the contact force causes the cantilever to *deflect* to accommodate changes in topography [107]. In the standard constant force mode, a feedback system maintains the cantilever deflection at a constant level (which corresponds to a constant force according to Hooke's law). The setpoint, a parameter, which is defined by the user, defines the force that will be exerted on the surface by the tip (which can be as low as ~ 0.1 nN). A common way to measure the cantilever deflection is by utilizing a laser beam which is reflected off the back of the cantilever, *via* a mirror, into a position-sensitive photodetector. The laser beam which bounces off the cantilever functions as an optical lever arm, amplifying the deflection. As the sample is scanned under the tip, the x, y and z position of the sample surface with respect to the tip is determined by a piezoelectric tube scanner. The movement of the sample in the z-direction, that is needed to keep the deflection at its constant setpoint level, is registered during x-y scanning, and a three dimensional map is constructed which is closely related to the topography of the surface. The block diagram in Fig. 3.2 (black lines) illustrates the essential components of the continuous contact mode AFM.

Frictional force, exerted by the sample on the tip as it sweeps over the sample, may significantly contribute to the topographical image [108]. Surface domains with different frictional properties may appear as topographical features in the image. The use of a four-segmented photodetector gives the advantage of being able to distinguish friction from topography, and with such a setup, lateral force microscopy can be performed.
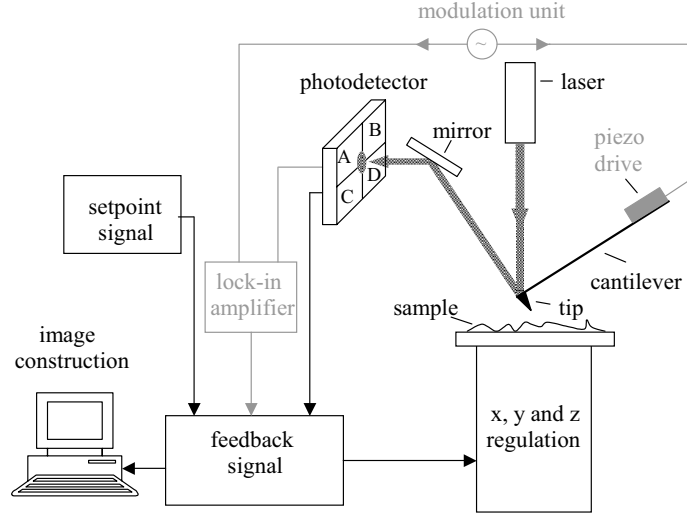
Fig. 3.2: *Block diagram of the essential components of the continuous contact (all black) and tapping (black with the additional gray units) mode AFM. A detector consisting of four photodiodes is shown. Scanning perpendicularly to the long cantilever axis (⊥ to the plane of the picture) the (A+B)-(C+D) signal gives topographical data, while the (A+C)-(B+D) signal responds to friction due to torsion of the cantilever, providing lateral force information.*

Contact mode successfully performed many pioneering AFM applications; however, it suffers from several drawbacks. The constant downward force of the tip onto the surface is not always low enough to avoid damaging certain sample surfaces. These include not only biological surfaces and most polymer surfaces, but even many seemingly harder materials, which are not completely resistant to such damage. In ambient operation, there is often a lack of force control in the desired range. The main reason for this is that, in a typical atmospheric ambient environment, surfaces are always covered by 10-30 monolayers of adsorbed water vapor, hydrocarbons and/or other contaminants. When the tip comes in close proximity to the surface the capillary action pulls the tip down towards the surface. This leads to increased normal and lateral forces when scanning in the continuous contact mode. Interaction forces as well as certain nanomechanical properties of the surface can be estimated by plotting so called force-distance curves [109].
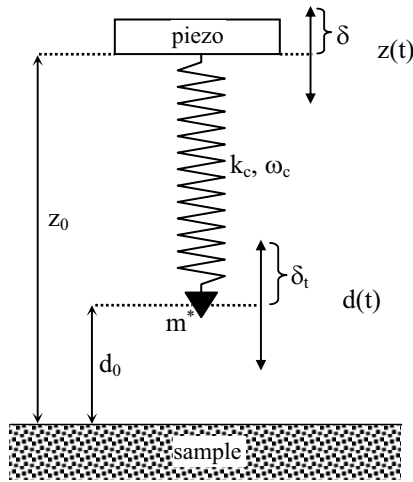
3.1.2 Tapping mode AFM

Tapping mode (TM) AFM [110, 111] successfully overcomes many drawbacks of the contact-mode. In tapping mode, to diminish lateral and normal forces exerted by the tip on the sample, the tip is brought only intermittently into contact with the surface during scanning. The basic idea is that the cantilever is brought into *oscillation*, and changes in oscillation amplitude or phase are detected as the vibrating tip sweeps across and interacts with the surface.

TM-AFM operation can be simulated as a driven, damped harmonic oscillator with an additional term to describe the interaction between the tip and the sample. The motion is expressed in terms of the displacement of the tip *d(t)*, and the position of the root of the cantilever *z(t)*, as depicted in Fig. 3.3. The cantilever is treated as a massless spring of spring constant k_c and eigenfrequency f_c that is loaded by a tip of effective point mass m^*. The equation of motion can be given as [112]:

$$m^* \ddot{d}(t) = k_c (z(t) - d(t)) + \frac{m^* \omega_c}{Q} (\dot{z}(t) - \dot{d}(t)) + F_{ts}(d, \dot{d}) , \quad (17)$$

where $\omega_c = 2\pi f_c$. The term $F_{ts}(d, \dot{d})$ contains the unique physics of the intermittent contact mode and represents the interaction between the tip and the sample. Q is the quality factor of the cantilever. (Q is defined as the ratio of the peak height of the root-mean-square (RMS) amplitude curve at resonance to the peak full-width-at-half-maximum.)

Fig. 3.3: *Driven, damped harmonic oscillator model system applied for the description of the tapping-mode AFM operation. See text for details.*

The cantilever is driven through *z(t)* as:

$$z(t) = z_0 + \delta \cdot \sin(\omega t) \qquad (18)$$

where δ is the drive amplitude and $\omega = 2\pi f$ with the drive frequency *f*. z_0 is the mean distance between the base of the cantilever and the sample surface, and it is used to regulate the setpoint amplitude. After a short transient, the oscillation of the tip can be expressed as:

$$d(t) = d_0 + \delta_t \cdot \sin(\omega t + \alpha) \qquad (19)$$

where d_0 is the mean distance between the tip and the sample surface, δ_t is the amplitude and α is the phase.

In TM-AFM the tip is mounted on a rigid cantilever ($k_c = 20$-50 N/m) that is oscillated vertically at a relatively high amplitude ($\delta = 10$-100 nm) by using a piezoelectric crystal. The oscillation frequency is set close to the mechanical resonance frequency of the cantilever ($f_c \approx 200$-400 kHz). Typical operation parameters give the cantilever enough energy to avoid being trapped by attractive forces. The movement of the tip goes through non-contact and contact tip-sample conditions and the two regimes are separated by the interatomic distance (a_0). For distances larger than a_0 the attractive tip-sample interaction (F_{ts}) can be calculated through the VdW force between a sphere and a flat surface according to Eqn. 15. At distances smaller than a_0 repulsive forces come into play and the description of F_{ts} in this regime is not that simple. Several continuum contact mechanical models have been proposed where both elastic and inelastic tip-sample interactions are considered as the tip touches the surface [112].

During tapping mode imaging the vibrational characteristics – the frequency, amplitude and phase - of the oscillating tip are measured. In principle a feedback regulation can be based on the detection of any of these parameters, since *via* Eqn. 17, these all are sensitive to changes of the tip-sample interactions. Most often it is the RMS oscillation amplitude that is measured, using the same detection device as shown for the contact mode. While the sample is scanned under the vibrating tip a feedback loop adjusts the tip-sample separation to maintain a constant cantilever amplitude at a setpoint level determined by the user. A topographical image of the surface is created by recording the feedback signal which regulates the vertical movements of the sample during scanning (and therefore contains height information), and plotting it as a function of the horizontal position, determined by the *x* and *y* positions of the piezoelectric tube scanner.

An alternative (maybe more picturesque) way of understanding the operation of the tapping mode is by considering, that under the influence of

the force gradient $(\partial F_{ts}/\partial z)$ near the surface, the cantilever behaves, as it would have a modified spring constant:

$$k_c' = k_c - \frac{\partial F_{ts}}{\partial z} \qquad (20)$$

As the tip approaches the sample, the change in the apparent spring constant will modify the cantilever resonance frequency too, since $\omega_c = \sqrt{k_c/m_{eff}}$ and therefore

$$\omega_c' = \omega_c \sqrt{1 - \frac{1}{k_c}\frac{\partial F_{ts}}{\partial z}} \qquad (21)$$

The modification of the resonance frequency will result in a change in the probe's oscillation amplitude, and the phase shift as well. The frequency dependence of the oscillation amplitude and phase is illustrated in Fig. 3.4.
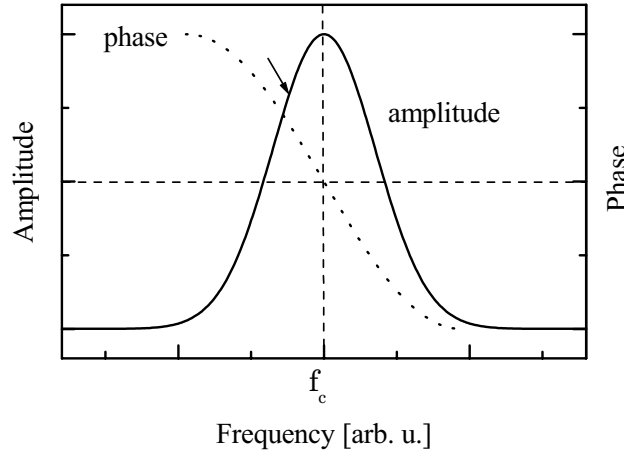
Fig. 3.4: *Frequency response of a typical TM-AFM cantilever. The amplitude of the tip vibration as a function of the driving frequency exhibits a peak that indicates the resonant frequency. The dashed line shows the phase of the tip oscillation. The arrow indicates a typical choice of drive frequency during TM-AFM operation.*

3.2 Artifacts

It is important to keep in mind that the AFM technique is subject to a number of artifacts that may appear in the images obtained. When interpreting images one has to remember that by scanning the tip across the sample AFM maps the tip-surface interaction forces or force gradients, which is then related to topography. The tip-surface interaction potential may be altered by peculiar local conditions yielding faulty height values. For example a sudden change in the thickness of the adsorbed water layer, or a change of the elasticity of the surface, or local charges may affect tip-sample interaction forces and in turn will appear as height data in the image.

It must be pointed out that many of the AFM methods are partially sensitive to non-topological aspects of tip-surface interaction. In recent complementary studies of ion induced surface defects by tapping mode AFM and shadow-replica electron microscopy a considerable discrepancy has been observed in the height measurements [113, 114]. The possible dependence of tapping mode AFM imaging on the physical or chemical properties of the ion impact sites calls for caution when interpreting images.

Both in tapping and in contact mode since the imaging process involves the tip "touching" the surface, the most common artifact is induced by the shape of the tip. All features on the surface will appear broader than they are, because of the size of the tip, while small features may hide in the "imaging shadow" of a higher feature in close proximity. Similarly, an indentation in the surface will appear less deep in the image when the tip end-radius is larger than the radius of curvature of the indentation. Also tips are not always spherical, which results in "reverse imaging", wherein all features show the characteristic orientation and shape of the damaged tip.

4. Experimental

The main experimental methods applied will be briefly outlined in the following. For more details the reader is referred to the respective articles.

4.1 Target preparation for ion-induced sputtering and surface modification studies

The choice of target preparation method for sputtering experiments depends on the substance and on the desired surface smoothness and target thickness.

Amino acid *L-valine* (chemical formula: $C_5H_{11}NO_2$, $M_w = 117.1$, $\rho = 1.23$ g/cm^3) *crystal* targets were prepared by allowing droplets of a nearly saturated water solution of the molecules to dry on a polished silicon substrate. Leaf-like crystals with their {100} faces parallel to the substrate surface were readily formed [115]. The >10μm thick crystals show atomically flat terraces, which are ideal for AFM studies.

Langmuir-Blodgett (LB)-*film* preparation [116] is a more complicated method which can be applied for preparing well-ordered layers of fatty acids with controlled thickness on a target substrate. A submonolayer of the fatty acid is deposited onto a very clean water surface. The water should be properly buffered and should also contain $CdCl_2$ in order to obtain a more stable film. Subsequently, the surface area is reduced and the surface pressure is increased until a solid monolayer of the fatty acid salt is formed. The molecules then "stand" with their hydrophilic end at the water surface. By repeatedly raising and dipping a polished, cleaned, hydrophilic silicon substrate through the fatty-acid-covered water surface, while maintaining a constant surface pressure, a well-defined monolayer is transferred to the substrate at each surface stroke. The final thickness of the film can be estimated by multiplying the known thickness of one layer by the number of monolayers deposited. LB-films constitute a unique test target for sputtering experiments, since they comprise a layered material which can be "engineered" on the nanometer scale.

25

In *electrospray* [117] target preparation, an acidic solution of biomolecules is sprayed through and out of a narrow capillary by an applied electric field. The solvent evaporates from the droplets obtained during the spray, and a biomolecular film is formed on a substrate placed in front of the capillary. Several-micrometer-thick films [118] can be produced by this technique.

4.2 Irradiation

Most of the irradiations were carried out at the Uppsala EN-tandem van de Graaff accelerator. ^{16}O, ^{32}S, ^{63}Cu, ^{79}Br, and ^{127}I atomic ions accelerated to the same velocity (1.1 cm/ns) have been used. Before impacting the targets, the ions passed through a thin carbon foil in order to establish charge state equilibrium – the charge of the ion after passing some distance through matter will generally be different than the charge used by the accelerator. Without this measure, the ions will display a different and variable *dE/dx* in the near-surface region of their impact trajectory. By contrast, when ions are in charge state equilibrium, their energy loss will be approximately constant in the region near the surface and also, *dE/dx* values from standard tables can be used [119]. While the same velocity of the various incoming ions ensures constant track dimension (because the δ-ray electrons have the same range for all the ions), the energy density in the ion track is different for each type of ion (because *dE/dx* varies for the different ions). Incidence angles of 0°, 45°, 67°, 79°, and 84° with respect to the surface normal have been employed. Fluences were estimated to be in the range 0.5×10^9 to 2×10^9 ions/cm^2, and the observed areal surface defect densities were in fair agreement with the estimated fluences. This supports the idea that each surface defect is created by the impact of one ion. The irradiations by 2.83-cm/ns Xe ions were carried out at GANIL, Caen, France.

4.3 Mass spectrometry

Mass spectrometry (MS) is an analytical technique in which sample molecules/atoms are volatilized, ionized, and then separated in space or in time according to their mass-to-charge ratios (*m/q*). Both *m/q* and ion abundance (yield) are subjects of measurement. In connection with the collector experiments (see next chapter), we applied plasma-desorption-

ionization mass spectrometry (PDMS) with time-of-flight (TOF) mass analysis for sputtering yield measurements.

In TOF-MS, all ionic species are accelerated through a potential difference, U, to the same kinetic energy, and then are allowed to drift through a field-free region of length L before detection. The time t_{TOF} it takes for a species of mass M and charge q to reach the detector is $\propto (2U)^{-1/2}L(M/q)^{1/2}$. This relation between the t_{TOF} and M/q ratio allows direct determination of the ion mass if q is known [120].

PDMS utilizes the sputtering of secondary ions by incident fast heavy ions (with kinetic energies in the MeV range for atomic projectiles) as primary ions from an accelerator or from a fission fragment source [42]. The name "plasma" refers to the high energy density (corresponding to a temperature of $\approx 10^4$ K) that is formed in a small region around the MeV ion trajectory on a sub-picosecond time scale after the impact. For a detailed description of the applied PDMS set-up see [47].

4.4 Collector experiment

While ejected *ions* are easily detected by mass spectrometry, neutral molecules, the major fraction ($\approx 10^4$ times more) [54] of sputtered species are "invisible" for mass spectrometry.

The total yield, *i.e.,* the number of intact molecules (ions and neutrals) sputtered per ion impact, can be measured either by detecting the material lost by sputtering *at* the target, or by collecting the sputtered material *in front of* the target. The former method can involve the utilization of a quartz crystal balance, for instance, by which the mass loss from the target is observed as a frequency shift of the oscillator [121]. A quartz balance has a detection limit of about 1 ng, which can be a problem if the total sputtering yield is low. Furthermore, the heating and damage induced in the quartz crystal by the stopping incident ions (*i.e.,* the ions penetrate the sample and go into the quartz) probably introduce additional uncontrolled frequency shifts. Target surface sputtering and erosion can also be measured by techniques that are sensitive to the target thickness, such as Rutherford backscattering [122].

The collector method, applied in the studies presented in this thesis, has been first employed by Salehpour [54]. The collector could be turned either to face the target (irradiation position), or toward the grid of a TOF-MS (analysis position). First, while bombarding a target with a known current of fast heavy ions, the sputtered material is collected on a clean silicon plate located in front of the target. Then directly, without breaking the vacuum, the collector plate is turned to the analysis position, and a

PDMS spectrum of the collected molecules is taken. Now, we suppose that at low collector coverage the area of the molecular ion peak of interest in the mass spectrum, acquired from the collector, is proportional to the number of primary ions incident on the target [101]. Therefore this peak area can be employed as a *relative* measure of the total amount of molecules sputtered and collected [IV], [101].

The *absolute* total yield from a peptide target can be obtained by immersing the entire collector plate in an acidic solution, thereby removing all the collected material from the surface to the solution and hydrolyzing the peptide molecules. Then a standard procedure of amino acid analysis [123] will give the amount of collected material [54].

In general, collector surfaces would be characterized by a sticking probability P, which is unknown. When a collector is placed in front of a target, bombarded with a number N of incident ions, and the absolute amount (α) of sputtered intact molecules is detected by amino acid analysis, an estimate of the total yield (Y_0) is $\alpha/(NP)$. However, since P is typically unknown, the quantity α/N is an approximation of the lower bound of Y_0. Additional error would be introduced in the total yield estimation if the angular distribution of the ejecta is unknown and the collector does not cover all sputtering angles. In the presented work we probed only the *relative* total yield of sputtered molecules at various fluences and hence the value of the sticking probability and angular distribution was of limited importance.

Since the target is damaged during irradiation, the total yield of intact molecules decreases exponentially as a function of the fluence (ϕ) *i.e.,* the number of incident primary ions per unit target area. The damage cross section provides more evidence for the spatial scale of matter affected by the impact of an energetic ion. Moreover, in certain experiments in which it is necessary to acquire qualitative information over a lengthy time interval, over which signals decline due to this damage, knowledge of the damage cross section allows one to carry out corrections which improve the validity of the final quantitation.

Damage cross sections for the peptide LHRH (Luteinizing Hormone Releasing Hormone, $M_W = 1182$ u) for primary ion beams with the same velocity, but different stopping powers *(dE/dx)*, have been calculated (III, IV).

4.5 Preparation of WO$_3$ nanoparticle films

The nanoparticles were generated by the so-called gas-deposition technique [61]. The main parts of the gas-deposition system applied are shown in Fig. 4.1.
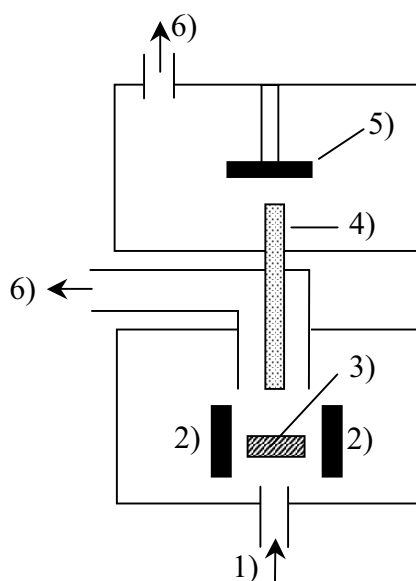
Fig. 4.1: Schematic of nanoparticle deposition by the gas-deposition technique. A solid metal precursor (3) is placed inside an induction coil (2) and is heated up to a high temperature in the evaporation (lower) chamber. A high purity cooling gas (He or Ar) is introduced (1) beneath the heated metal piece, and flows upwards. Single nanoparticles, formed in a condensation process, are transferred into the deposition (upper) chamber via a transfer pipe (4) and are deposited onto a substrate (5). Agglomerated particles and excess gas are removed through separate exhaust pipes (6).

During gas-deposition a metal of interest is evaporated or sublimated in the evaporation chamber by heating it up to a temperature that can be as high as ~ 2000ºC (depends on the material). While heating the metal pellet, a flow of high purity cooling gas (typically He or Ar) is introduced underneath it. As the gas-flow transports the metal vapor upwards, the vapor cools down. First clusters of atoms, and then single ultrafine particles are condensed. Since the particles are condensed from a hot vapor in course of gradual cooling, the particles are in crystalline form (nanocrystals). Further upstream, chain- and fractal-like agglomerates can be formed due to the collisions of the nanoparticles. However, the transfer pipe is placed in such a region of the condensation volume where *single* nanoparticles are present. The single nanoparticles are quickly led to the deposition chamber through the transfer pipe, and thereby agglomeration is avoided.

By this technique, individual nanoparticles with a narrow size distribution can be deposited onto a substrate placed in the upper chamber. The width of the size distribution depends on the total gas-flow and it can be ± 15% of the mean size. Generally, nanoparticles in the nm size range can readily be generated. The mean particle size can be regulated by the deposition parameters. However, even at the same adjustments the mean particle size may slightly vary due to the uncontrolled nature of the sublimation rate at the pellet surface if a material with high melting point is applied.

Applying a nozzle, the pressure difference between the two chambers gives rise to high speed of the particles - up to several hundreds of

m/s – and therefore compact materials are formed. Any kind of metal nanoparticles can be generated on this way, provided that a sufficient vapor pressure is built up.

The introduction of oxygen (O_2) (*i.e.,* a reactive gas) together with the cooling gas results in the oxidization of the metal atoms either in the gas phase or on the surface (provided that the metal has an oxide form). This, so-called, reactive gas-deposition technique is a suitable means for the formation of WO_3 nanoparticle/nancrystalline deposits. Tungsten-oxide (WO_3) has a much lower melting point than tungsten (W), therefore a sufficient sublimation rate of WO_3 can be achieved for the production of WO_3 nanoparticles at the temperatures applied.

To produce WO_3 nanoparticle films, a tungsten pellet was heated up to ~ 1100-1200ºC. Synthetic air (80% N_2 and 20% O_2) was introduced beneath the pedestal at a mass flow of 10 l/min, and the pressure in the evaporation chamber was set to 20 mbar. The transfer pipe was 3 mm in diameter.

The particles were deposited onto an Al substrate, positioned 3 cm above the end of the transfer pipe in the deposition chamber. The substrate was translated at a constant speed of 2 mm/s above the transfer pipe and WO_3 nanoparticles were deposited along a stripe. Due to diffusion and to the velocity profile of the carrier gas nearby the substrate, the thickness of the deposit was non-constant. The film thickness was recorded by a Tencor Alpha-Step 200 mechanical stylus profilometer. The thickness above the transfer pipe was 150 nm, that was gradually decreasing perpendicularly outward from the deposition line [VII].

4.6 Atomic force microscopy

SFM studies were performed under ambient conditions on two commercially available instruments. During the very first experiments a TopoMetrix-2000 (TopoMetrix Corp., Santa Clara, CA, USA) was employed in the conventional continuous contact mode. The silicon nitride tips employed have a radius of curvature ≈ 10 nm and cone angle < 6°. Later on, a Nanoscope III (Digital Instruments, Santa Barbara CA, USA) was employed, operated in the intermittent contact or tapping mode[TM], in order to reduce surface distortion during imaging. For tapping, etched silicon probes with a nominal radius of curvature of ≈ 10 nm, and cone angle 36°, located on an I-shaped cantilever, were used. In this mode, the tips were oscillated by the cantilever with an amplitude < 100 nm at a frequency close to its resonance frequency (≈ 300 kHz). Images were analyzed with Nanoscope III software.

AFM provided a unique means for *direct* observation of (though at long times) the ion-induced surface tracks. Whereas the general appearance of the defects has implications for the possible sputtering mechanisms, the approximate crater volumes allowed one to estimate the *total sputtering yield* of various organic materials for different incident ions.

AFM images of WO_3 nanoparticle films revealed the formation of agglomerates during the deposition process. Additionally, the influence of some of the scanning parameters on the appearance of the particles could also be investigated.

5. Results and discussion

Motivated both by fundamental and practical considerations, two sorts of nanostructures have been examined by atomic force microscopy. (I) Energetic-ion-induced surface tracks have been studied in order to achieve a better understanding of the electronic sputtering of organic solids, and (II) deposits consisting of WO_3 nanoparticles were investigated for studying the agglomeration of the nanoparticles. Meanwhile some interesting aspects of the TM-AFM were also investigated.

5.1 Morphology of surface tracks on L-valine crystals

On the surface of *L-valine crystals*, for grazing incidence [127]I ions, a trench followed by a raised bulge on the surface commonly occurred. Such features were generally followed by a diffuse raised tail extending a rather long distance over the penetrating ion track, oriented in the direction of the ion incidence azimuth (Fig. 5.1 left), [I]. For angles of incidence approaching the surface normal, the tails and bulges became shorter and eventually disappeared, and the trenches became shorter (Fig. 5.2), [II]. For normal incidence, round craters accompanied by faint raised rims were apparent (best seen in Fig. 5.1 right).

Our observations are in qualitative agreement with electron-microscope replica measurements of craters induced in gypsum by grazing incidence 100-MeV [132]Xe ions [124].
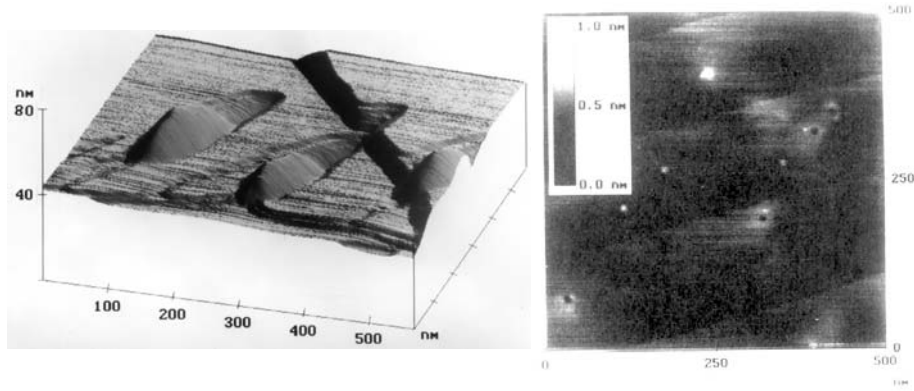
Fig. 5.1: *Tapping-mode AFM images of L-valine single crystals irradiated by 78.2-MeV ^{127}I ions at grazing angle of incidence (left) and at normal incidence (right).*

The linearly increasing length with $cos(\theta)^{-1}$ is in good agreement with the predictions of the pressure pulse or shock wave models, while according to these models the width should be completely independent of the angle of incidence, at variance with our observations (Fig. 5.2).
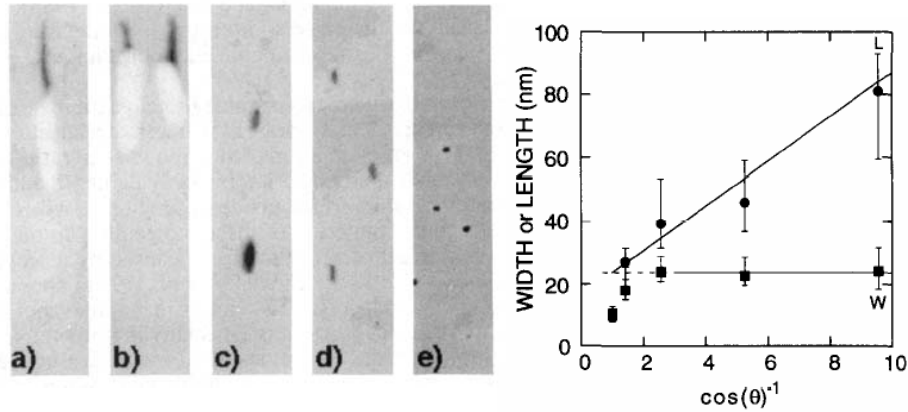
Fig. 5.2: *a)-e): Tapping-mode AFM images of representative defects created in L-valine surfaces by ^{127}I ions incident at 84°, 79°, 67°, 45° and 0° (i.e., normal incidence). Right: crater length (L) and width (W) plotted against $cos(\theta)^{-1}$, where θ is the angle of incidence with respect to the surface normal.*

Owing to the low effective tip-surface contact forces (~ 1-10 nN) employed in tapping-mode AFM, the images were attributed to genuine topography, rather than to other material aspects such as spatial modulations in surface elasticity. The latter situation has been observed on energetic-ion-irradiated mica surfaces by continuous-contact-mode AFM [125], lateral force microscopy [126] and force modulation [127] studies. The consistent

33

observation of subfeatures of inverse curvature in close proximity (*e.g.* craters versus rims and raised tails) in two different AFM imaging modes seems to rule out this possibility in our studies.

Early work showed that L-valine craters were distorted in the probe tip scanning direction in the continuous repulsive contact mode, and that the distortion was drastically reduced when using the tapping-mode [I]. However, a more extensive study showed, that the detailed appearance of the craters depended on how the tapping-mode operating parameters were selected. The apparent dimensions of the craters were especially susceptible to the drive amplitude adjustment [III], [113]. This suggests that even in the tapping mode, some distortion of the sample takes place.

In addition, the AFM probe tips employed had a nominal curvature radius of 10 nm, which means that the ability of the probe tip to sample a deep crater was inherently limited. However, it is reassuring that the trend observed in the data qualitatively persists to much higher stopping powers than what we applied, for which the craters are larger and the imaging is probably less susceptible to AFM artifacts [128]. It can be concluded that the numerical dimensions of the observed craters are semiquantitative in nature.

Our observation of permanent plastic deformation associated with each ion track (raised tails, bulges and crater rims) can best be interpreted in terms of "hydrodynamic"-type models, like the pressure pulse and shock wave models. In such models, either a Coulomb explosion in the ionized track, or a physical expansion of ultratrack molecules due to vibrational excitation by δ electrons, causes a pressure pulse, or a volume force. Such forces initiate sputtering and crater formation where the ion track crosses the vacuum interface. As the ion penetrates into the bulk, crater formation ceases, but a volume force can still give rise to the observed plastic deformation. By contrast, molecule-by-molecule evaporation characterizing thermal spike models cannot explain raised deformations on the surface.

5.2 Sputtering yield as a function of the deposited energy density

5.2.1 Ion-induced craters in L-valine probed by AFM

The dependence of defect dimensions on $(dE/dx)_e$ for $\theta = 79°$ grazing angle of incidence had been examined. Trenches became shorter and more shallow with decreasing $(dE/dx)_e$. Crater volume estimated from

profiles of the images scaled as $(dE/dx)_e^n$, where n was in the range 3 to 4. However, one should point out that at low $(dE/dx)_e$ the volume determination is quite uncertain due to the small size of the craters (see Fig. 5.3) relative to the nominal end-radius (~ 10 nm) of the probe tip and crater volumes may be underestimated. Therefore the conclusion that the exponent n is in the range of 3 to 4 could be an overestimation. The corresponding crater width (W) and length (L) scaled as $(dE/dx)^{0.44}$ and $(dE/dx)^{0.77}$ respectively (Fig. 5.3).

The obtained *crater volume scaling* with $(dE/dx)_e$ is in good agreement with the third power scaling law, that has previously been obtained by collector experiments for the amino acid leucine [101]. Also the pressure pulse and shock wave models predict that the neutral sputtering yield scales as $(dE/dx)^3$ (Eqn. 7) [93]. However, considering that L-valine is a small, volatile organic molecule, thermal evaporation may also be an effective sputtering mechanism if the coupling of energy into vibrational modes of the desorbed species is inefficient [90] (*i.e.,* if no fragmentation occurs). For sufficiently large $(dE/dx)_e$, the thermal spike model predicts that the yield scales as the second power of $(dE/dx)_e$ (Eqn. 5), but for lower $(dE/dx)_e$, it has been shown that a steeper dependence on $(dE/dx)_e$ could hold if the initial distribution of thermal energy has a finite width [88]. Therefore, in this later situation the thermal spike model could also describe the observed crater volume $(dE/dx)_e$ scaling law.

The obtained scaling of the *lateral crater dimensions* with $(dE/dx)_e$ could be in agreement with both a square root dependence predicted by an evaporative spike model, (Eqn. 9), considering $W \propto (dE/dx)^{0.44}$, and a linear dependence predicted by the pressure pulse model (Eqn. 8), considering $L \propto (dE/dx)^{0.77}$. However, the observed crater length-to-width ratios deviate from the predictions of both models. For 79° angle of incidence the crater length is predicted to be $1/\cos(79°) = 5.2$ times the width, whereas the observed length-to-width ratios are ≤ 2.4.

The surface track areas displayed a linear to slightly superlinear dependence on $(dE/dx)_e$ [Fig. 4 in IV], that correlates better with the thermal spike prediction than the $(dE/dx)_e^2$ scaling, predicted by the pressure pulse and shock wave models.

So, based on the observed crater size dependence on $(dE/dx)_e$, we could not clearly distinguish which sputtering mechanism holds for L-valine, considering pressure pulse/shock wave or thermal spike models. However, further modeling, with consideration of the emission of clusters and the strong binding anisotropy in the layered crystals of L-valine, can explain at least some of these trends within the framework of pressure pulse and shock wave models [129], [III].
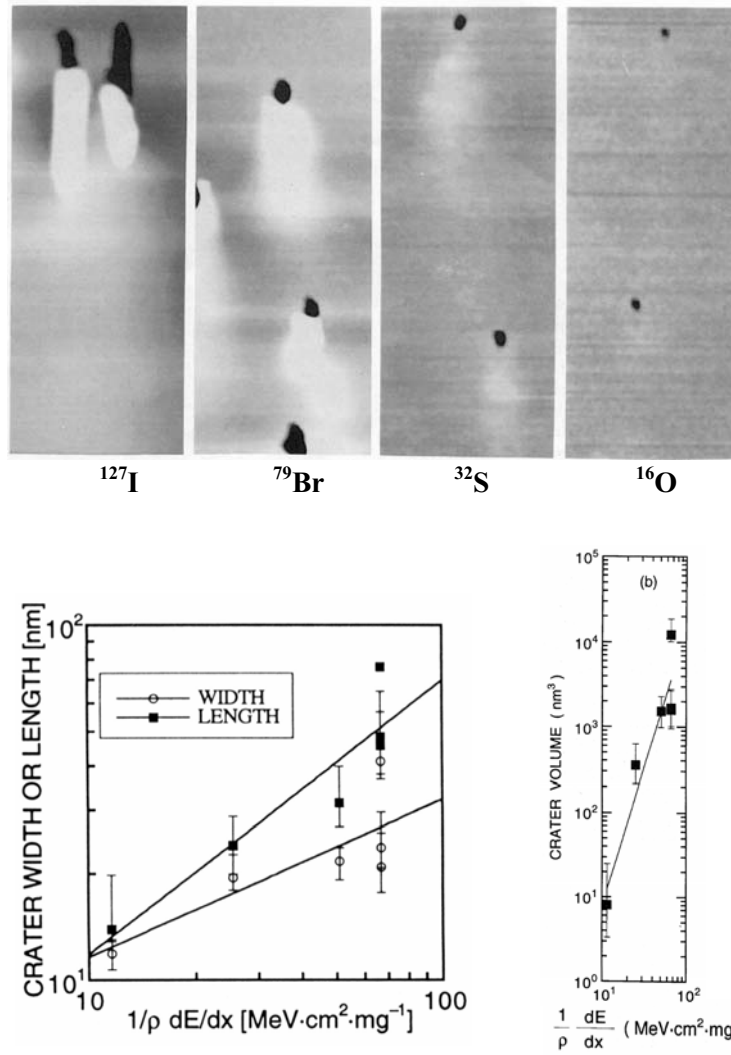
Fig. 5.3: Top: *AFM images of L-valine surface defects induced by 0.61 MeV/u ^{127}I, ^{79}Br, ^{32}S and ^{16}O ions incident at 79° grazing angle.* **Bottom left**: *L-valine crater widths (W) and lengths (L) measured by AFM as a function of the electronic stopping cross section of the incident primary ions.* **Bottom right**: *L-valine crater volume plotted against electronic stopping cross section. The lines represent least squares fits to a power law.* $W \propto (dE/dx)_e^{0.44}$; $L \propto (dE/dx)_e^{0.77}$ and $Vol. \propto (dE/dx)^{3.2}$.

5.2.2 Relative total sputtering yield measured by collector experiments

The relative total yield of intact LHRH molecules determined by *in situ* collector experiments scales with the electronic stopping power of the incident ion as $(dE/dx)^{3.4}$ (Fig. 5.4) [IV]. Hence the sputtering of LHRH deviates from evaporative heated spike model predictions of $Y \propto (dE/dx)_e^2$ [45, 89], and agrees better with the $Y \propto (dE/dx)_e^3$ scaling, predicted by the pressure pulse and shock wave models and by molecular dynamics simulations [87, 91, 97].
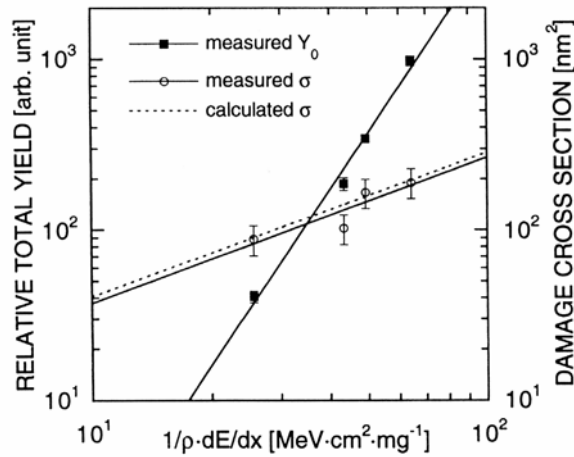
Fig. 5.4: *The relative total yield and damage cross section of LHRH, determined by collector experiments as a function of the electronic stopping power of the incident ion. $Y_0 \propto (dE/dx)_e^{3.4}$ and $\sigma \propto (dE/dx)_e^1$. The dashed line is the result of multiple-hit theory calculations assuming that the target molecules are damaged if they are hit by at least one δ-electron (for details see paper IV).*

5.2.3 Damage cross section

Target damage has been modeled by assuming that it could be related to the interaction of the δ-electrons with the target molecules. Multiple-hit theory [130] based on Poisson statistics provided a simplified approach to describe this interaction [IV]. We found that the $(dE/dx)_e$ dependence of the damage cross section (σ) is linear for the total sputtering of LHRH as determined by collector experiments (Fig. 5.4) [IV].

The fact that the total yield of intact material sputtered by fast atomic ions grows faster with $(dE/dx)_e$ than the damage cross section (cubic and linear respectively in Fig. 5.4) suggests that a larger fraction of the ejected volume is in the form of intact molecules for higher $(dE/dx)_e$ ions of the same velocity. Hence, if a large fraction of intact ejected material is desired, as for instance is the case in mass spectrometry applications, one would obviously try to employ as high $(dE/dx)_e$ ions as possible. However, only a factor of two higher stopping power than for [127]I ions, used here, can be achieved by employing the heaviest possible atomic ions ([238]U). More gain on $(dE/dx)_e$ can also be obtained by increasing the velocity, which unfortunately increases the range of the damaging electrons and hence σ (according to the hit model) as well.

Nevertheless, by using *cluster* ions, a higher $(dE/dx)_e$ can be reached at even lower velocities than what has been employed in this thesis for the atomic ions. Indeed, a 20-MeV C_{60}^+ ion can generate giant crater volumes in an organic solid [128, 131]. The electronic stopping power of this ion is large while the range of the δ-electrons is short due to the relatively low ion velocity. It has been demonstrated experimentally that for a sample, consisting of trypsin molecules, the secondary molecular ion emission yield is about two orders of magnitude larger in case of 20-MeV C_{60}^+ primary ions than with MeV atomic ions [132].

5.3 Sputtering from layered materials

Layered materials, such as L-valine or Langmuir-Blodgett (LB) films, have anisotropic binding properties, which must be considered when modeling their ejection mechanism during the sputtering process.

AFM imaging of LB-films was challenging, since the operation parameters of the microscope must be adjusted for very gentle tapping, in order not to disrupt these soft surfaces. On LB-films of arachidic acid irradiated at grazing incidence, elongated craters were clearly observed (Fig. 5.5). Craters were often followed by a short hillock on the surface located over the bulk ion track. The crater dimensions depended on how the tapping mode was operated, but qualitatively the craters on the LB-film were somewhat narrower and longer than on the L-valine crystals for the same incident ions.

Previous PDMS studies of sputtered ions from a marker layer (*i.e.,* a layer composed of molecules of unique mass located at a controlled depth in the LB-film) implied that material is sputtered from a depth of at least the depth of the marker layer [133, 134]. Based on these experiments, deeper (10-30 nm) craters were inferred than what we have observed by AFM (2-

7 nm) [V]. This variance could be either due to the limited accuracy of the AFM when deep and narrow features should be imaged, or else due to the filling of the caters in the course of some long-time processes. Attempts have been made to explore what simple sputtering models predict about crater formation in a comparison between LB-films and L-valine crystals.
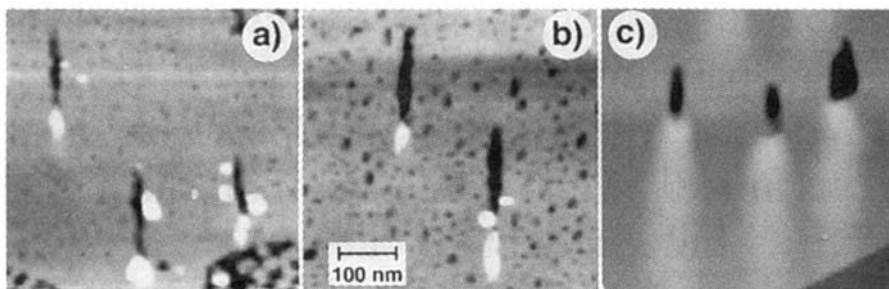
Fig. 5.5: *AFM images of craters induced in organic surfaces by 48.6-MeV ^{79}Br ions incident at 84° with respect to the surface normal. Each figure is 500×500 nm^2, and ions are incident on the surfaces from the top of the images. (a,b) LB arachidic acid target probed by TM-AFM with different drive amplitudes. Image b) was taken with ~8× higher drive amplitude than image a). (c) L-valine single crystal probed by TM-AFM.*

The *evaporative thermal spike model* can explain the relative narrowness of the LB-craters with respect to the L-valine craters only by assuming thermal equilibrium during the spike [V]. However, thermal equilibrium might not be established on the time scale of the spike. Moreover, according to this model, the wider L-valine craters should be similarly longer than the LB-craters, which was not observed.

However, ion sputtering data from LB-films have been previously rationalized by a thermal spike model [134]. Also, monomer ion ejection patterns from L-valine display a normally peaked cosine to over-cosine thermal-type polar angle ejection distribution [48]. For a series of atomic ions incident on L-valine, crater width scales roughly as *(dE/dx)$^{0.5}$* [II], in agrrement with the thermal spike model.

According to the *pressure pulse model,* craters in LB films are predicted to be about 1.8 times as wide as craters in L-valine crystals, also at variance with our observation.

Nonetheless, in all cases studied, raised bumps on the surfaces over the inwardly-penetrating ion tracks suggest the occurrence of a hydrodynamic pressure pulse acting radially outward from each ion track [I,

39

II]. Also, from collector experiments [IV, V], [101], neutral ejecta yields are observed to scale as *(dE/dx)^3*, in good agreement with the pressure pulse models.

An adjustment to the pressure pulse model was considered, which gave better agreement with the crater width measurements [129]. According to this modified PP model, if target material is emitted as *clusters*, the effective binding energy per cluster atom (or molecule) is reduced, and larger crater radii can be expected relative to the situation in which individual atoms (or molecules) are emitted. It has also been shown that the propensity to form clusters could depend on the ion angle-of-incidence [129].   For normally incident ions, variations in energy density and transferred momentum are most severe just at the surface around the ion impact point, so the material stress is highest there, and hence the degree of clustering would be expected to be rather small. Mostly single molecules and small clusters would be emitted. For grazing incidence ions, which travel below and almost parallel to the surface, the opposite situation occurs. Near the surface under which the ion has penetrated to a significant depth, variations in the energy density and transferred momentum are small, and clusters can be much bigger owing to the lower degree of stress in the crystal lattice.

The difference between crater widths observed in LB-films and L-valine crystals may be due to a difference between the clustering behavior in the two materials under the stress related to energy deposition by the incident ion. Exploring this possibility, simplified models were constructed [V] and crater shapes were estimated by the procedure given by [129]. It was approximately calculated how the binding energy is distributed in space for these two layered materials. The calculation suggests that the specific spatial distribution of the binding energy in the two molecular solids, and the emission of clusters, are important factors in determining the respective crater width. L-valine is much more tightly bound in the basal plane (target surface plane) than is an LB-film, implying that it is more energy-efficient to desorb wider clusters in the case of L-valine (Fig. 5.6) [V].

Evidence for sputtering of organic clusters has been obtained previously as well. Cluster ions are commonly observed in PDMS [135-137], and some of their characteristics are well described by pressure pulse sputtering [48, 49].
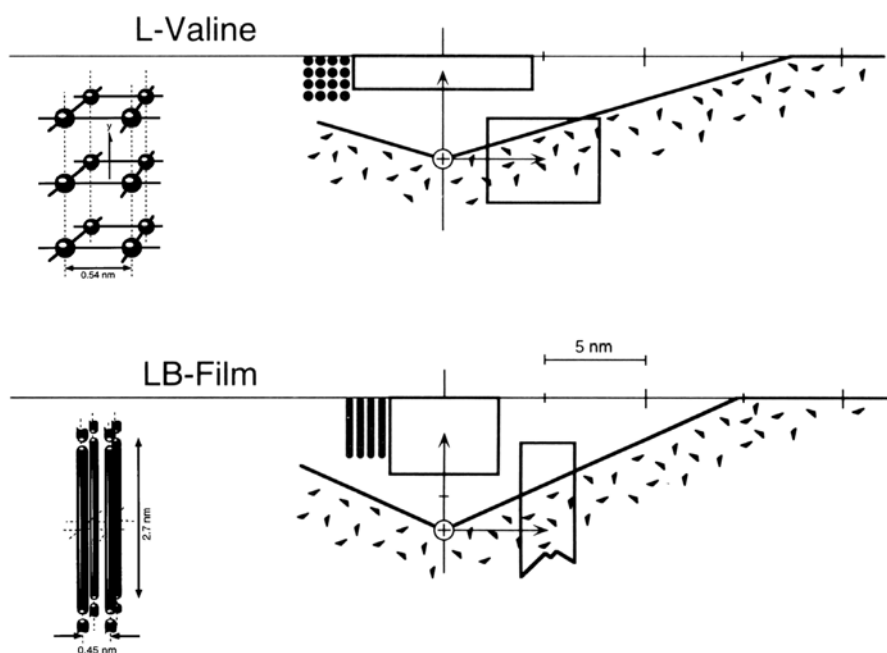
Fig. 5.6: *The geometry of clusters (open rectangles), that can possibly be sputtered from L-valine (top) and LB-film of arachidic acid (bottom) by grazing incident ions. The penetration points of the ions through the plane of the figure are denoted by plus signs. The geometries were calculated according to a modified pressure pulse model [129] with special consideration of clustering in layered materials with anisotropic binding energies. (For details see paper III).*

5.4 AFM studies of gas-deposited WO₃ nanoparticles

At low surface coverage (< 0.5 %), we observed single nanoparticles with mean size of 1.5 nm. An increase of the amount of the particles led to agglomerate formation, which appeared at surface coverages as low as 2 to 4%. At full coverage, the mean agglomerate size was ~ 5 nm (see Fig. 5.7 top line).

The size distributions of the single nanoparticles as well as of the agglomerates were found to be log-normal (see Fig. 5.7 bottom line). While the log-normal size distribution of the primary particles, *i.e.*, the gas-phase nanoparticles forming the deposit, is well understood [138], it is still not fully described how this distribution evolves to a log-normal form for the

agglomerates as the nanoparticle film is built up. Simulations of the agglomeration process showed relatively good agreement with the experimental observations, though with significant deviations from log-normality for the size distribution of bigger agglomerates [VII]. Possible improvements with the simulation are currently in progress.

The mean size of the agglomerates did not change as the sample was annealed at temperatures up to 250°C.
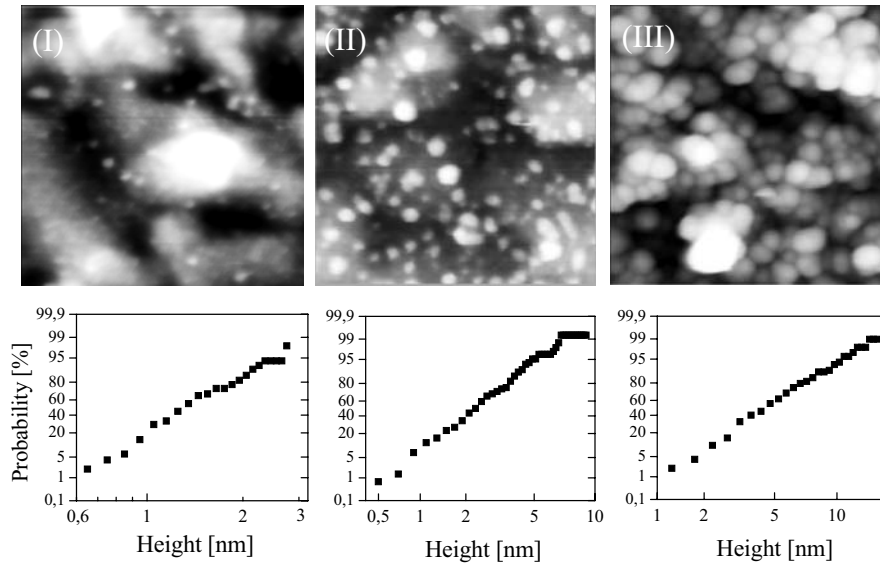
Fig. 5.7: Top: *AFM images of WO$_3$ nanoparticle deposits produced by gas deposition onto Al substrates. The amount of deposited particles increases from (I) to (III). The round features, which gradually icrease in size from (I) to (III), can be attributed to WO$_3$ particles or agglomerates of such particles, while the diffuse white areas (especially prominent in panel I) are natural large-scale undulations of the underlying substrate. The height scales — i.e., the vertical distance between the lightest and darkest regions — are 20, 25, and 80 nm for panels (I), (II), and (III), respectively. The depicted areas are 200 × 200 nm^2.* **Bottom**: *corresponding height-probability plots (each plot corresponds to the picture above it). The vertical scales in pane are cumulative probabilities in percent units. A linear relation corresponds to a log-normal size distribution in the chosen representation.*
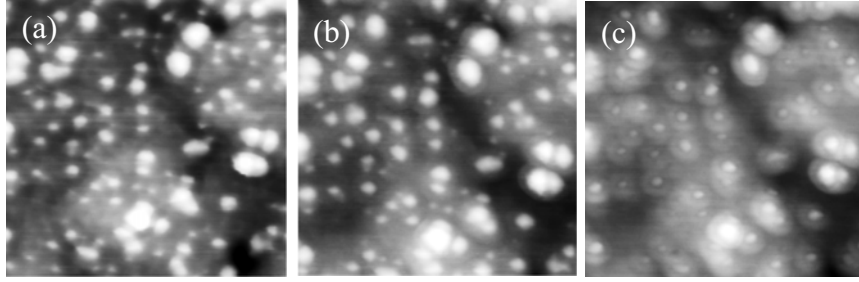
Fig. 5.8: *AFM images taken from the same 200 × 200 nm² area. This area was not fully covered by particles, but some agglomeration could be discerned. The free amplitude of the oscillating tip was 75, 45, and 25 nm in panels (a), (b), and (c), respectively. The height scale — i.e., the vertical distance between the lightest and darkest regions — is 20 nm.*
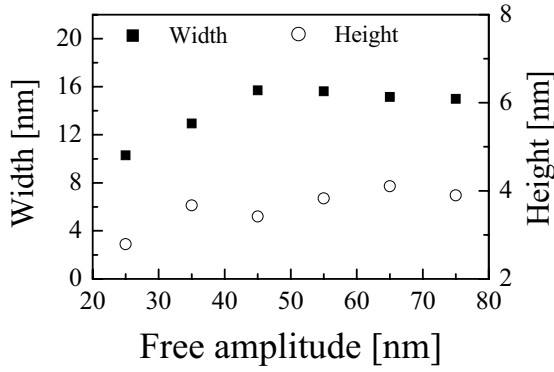
Fig. 5.9: *AFM data on the mean width and height of WO_3 nanoparticles as a function of the free amplitude of the scanning tip. The same tip was used, and the same 24 particles were measured, at each of the amplitudes. Analogous data were obtained in other experiments.*

AFM images of the nanoparticles were found to be sensitive to the free amplitude of the oscillating tip, thus indicating that the images were not purely topographical (see Figs. 5.8 and 5.9). In order to elucidate the underlying physical principles for this phenomenon, model calculations were performed. We focused our attention on the observed variance in the apparent nanoparticle height with the selected free amplitude of the scanning tip. The operation of TM-AFM was simulated by a driven, damped harmonic oscillator with an additional term to describe the interaction between the tip and the sample. The equation of motion was solved as the movement of the tip went through non-contact and contact tip-sample conditions [112]. Non-contact forces were considered as van der Waals forces, and contact forces were calculated according to the contact mechanical model of Maugis [139]. The Maugis model has the advantage, that it is applicable to various combinations of the tip-sample system

43

concerning adhesion and elastic properties. Simulations of the TM-AFM imaging of single nanoparticles with different free amplitudes of the oscillating tip were performed. Repeated simulations with various combinations of surface energies and elasticities of the tip and the nanoparticle (Fig. 5.10) indicated, that the *high adhesion forces* can cause the observed influence of the free amplitude on the apparent height of the nanoparticles on the images [VII]. The high adhesion forces could be attributed to the capillary forces that could be quite strong especially in ambient conditions. An expanded version of the simulation with separate consideration of the capillary forces is under development.
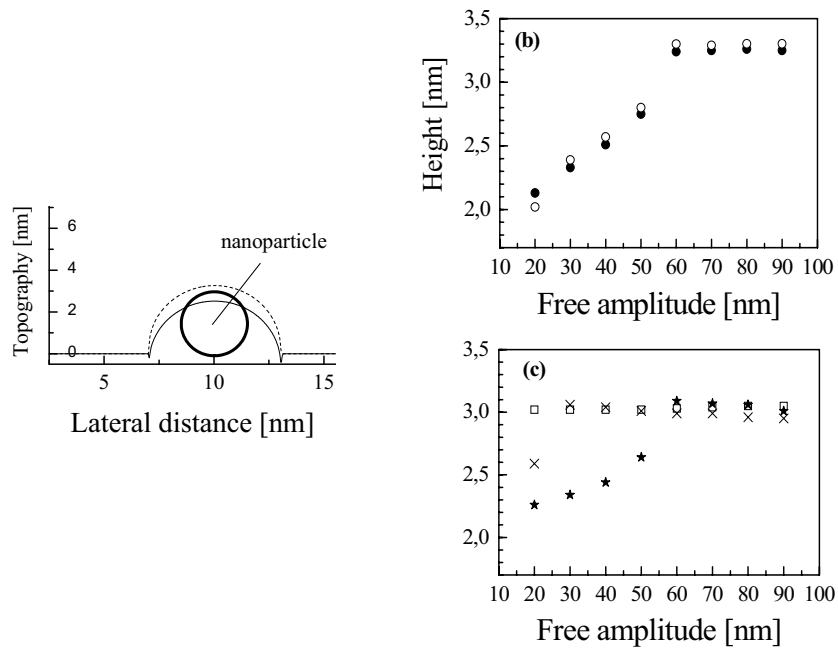
Fig. 5.10: Simulations of the imaging of a nanoparticle by tapping mode AFM. The diameter (i.e., height) of the particle was 3 nm. Panel (a) shows typical simulated response curves for the imaging of a WO₃ particle on an Al₂O₃ surface. The free amplitude of the tapping tip (A) was selected to be 90 nm (dashed curve) and 40 nm (solid curve). Panel (b) shows simulated WO₃ nanoparticle height vs. A for the surface energies of the particle being 7.2 J/m² (solid circles) 2.4 J/m² (open circles). Panel (c) shows simulated nanoparticle height versus A for an aluminum nanoparticle on an aluminum surface (stars) and for a WO₃ nanoparticle on a WO₃ surface (crosses); the open squares correspond to the height vs. A for a WO₃ nanoparticle on an Al₂O₃ surface, assuming a surface energy of 0.04 J/m² for the surface and the nanoparticle.

6. Concluding remarks

The work presented in this thesis was related to two "extremes" of nanometer scale surface tailoring: (I) the *carving* of surfaces by energetic ions and (II) the *building* of microstructures by spraying nanoparticles on a surface. The obtained nanostructures attract considerable interest in the expanding field of nanotechnology for future processing. Template formation by selective etching of ion tracks for the construction of metal nanowires, or WO_3 nanoparticle film coatings for gas-sensors are just two examples for the possible application areas of ion tracks and NP-films, respectively. The development of NT requires the characterization of the constructed nanostructures as well as the understanding of the physical phenomena underlying their formation. To this end atomic force microscopy has provided a unique means. While scanning the nanostructures, interesting aspects of the AFM imaging procedure were also observed. Investigations of the influence of certain scanning parameters on the apparent images can be valuable for the future application of AFM in nanotechnology.

6.1 Ion induced surface tracks

The view of the intersection of an ion track with a surface has elucidated the response of a material to a dense nanometer-scale track of deposited energy. Our observation of permanent plastic deformation associated with each ion track (raised tails, bulges and crater rims) can best be interpreted in terms of "hydrodynamic"-type models, like the pressure pulse and shock wave models. In such models, either a Coulomb explosion in the ionized track, or a physical expansion of ultratrack molecules due to vibrational excitation by delta rays, causes a pressure pulse, or a volume force. Such forces initiate sputtering and a crater formation where the ion track crosses the vacuum interface. As the ion penetrates into the bulk, crater formation ceases, but a volume force can still give rise to the observed plastic deformation (Fig. 6.1). By contrast, molecule-by-molecule evaporation characterizing thermal spike models cannot explain raised deformations on the surface.

The observed cubic electronic stopping power dependence of crater volumes and sputtering yields is also consistent with the predictions of the pressure pulse model and molecular dynamics simulations. Nevertheless, volatile amino acid targets can just as well be displaying evaporation of individual molecules from some crater regions, as suggested by the observed sublinear dependence of the crater width on the ion track energy density.

incident ion

$$\frac{\vec{F}}{Vol} = \vec{\nabla}\varepsilon(r,t)$$
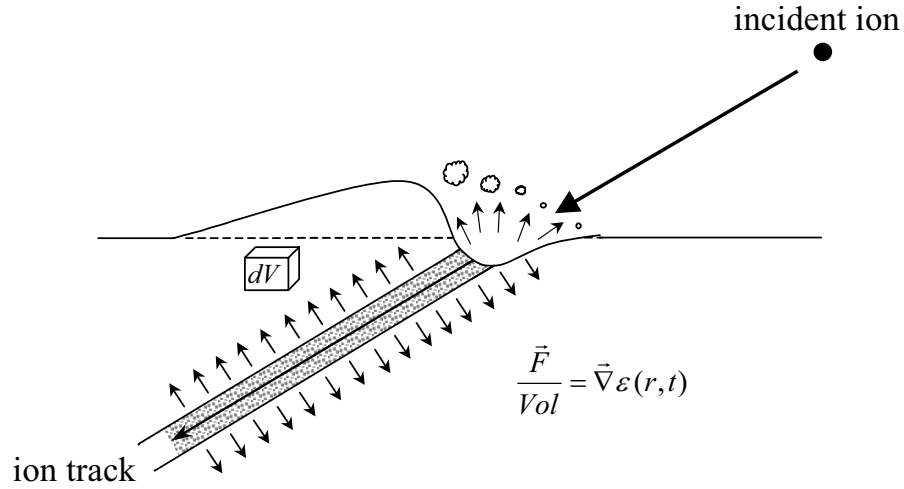
ion track

Fig. 6.1: *Schematic of sputtering and plastic deformation of a target due to a cylindrical pressure pulse created in the ion track region. Near the ion impact point, molecules are fragmented and fragment ions are ejected backwards along the incident ion direction. Where the energy density gradient is smaller but still sufficient to deliver the critical impulse to escape to some volume element of the target, intact molecules or clusters are ejected in a direction correlated with the ion track direction (away from the incident ion direction). The amount of sputtered intact molecules scales as the third power of the electronic stopping power. Further away from the ion track, the momentum acquired in the solid is too low for sputtering to occur, but the track expansion results in plastic deformation of the surface, in the form of a raised hump.*

Contrary to all model predictions considering the ejection of *individual molecules*, L-Valine craters are significantly wider for grazing ion incidence than for normal incidence. Moreover, craters induced in Langmuir-Blodgett films are narrower and longer than expected based on average molecular binding energies. Further modeling, with consideration of the emission of *clusters* and the strong binding anisotropy in the layered

46

crystals of L-valine and in LB-films, can explain some of these trends within the framework of pressure pulse and shock wave models.

A qualitative picture of the sputtering process as generated by an expanding cylindrical track is consistent with our observations of intact sputtered molecules and the ion induced surface tracks. However, the assumption of a *combined ejection mechanism* encompassing both the evaporative thermal spike and the pressure pulse model may have some basis.

In fact, measurements of the angular distribution of sputtered molecules [140] and molecular ions [48, 49, 51] together with damage cross section measurements [51, 140] indicate that near the ion track core evaporative processes are dominant and often strong fragmentation occurs, while further away from the ion impact site intact molecules or clusters can be sputtered in a direction correlated with the pressure pulse or shock wave created in the solid by the incident ion (see Fig.6.1).

In any case, however surface modifications and damage are viewed, it is apparent that energetic ions can serve as a means for creating nanometer-scale sites of altered structure and/or energy on a surface.

6.2 Nanoparticles

AFM images of gas-deposited WO_3 nanoparticle films revealed the formation of agglomerates in the course of the deposition process. Thus, gas-deposition can serve as a powerful means for building nanostructured materials. The observation that the size distribution of the agglomerates is log-normal just as is the size distribution of the primary particles forming the deposit is interesting from a basic point of view. Preliminary calculations indicate that the observed agglomeration process can well be simulated by simple model assumptions.

The mean agglomerate-size was stable as the sample was annealed up to 250°C. Therefore, below this temperature, WO_3 nanoparticle-films are suitable for sensor or other applications, where high thermal stability is required.

The observed influence of some of the scanning parameters on the appearance of the particles during TM-AFM suggests that AFM images should be interpreted with caution, and possible non-topographical contributions to the images should always be considered. On the other hand, the sensitivity of the AFM technique to local changes of various material properties (*e.g.*, elasticity, surface energy) along the surface gives the opportunity to measure these properties on the nanometer scale.

7. Outlook

During the past few years since I finished the work related to ion-induced sputtering, additional experiments have provided further insight into the electronic sputtering phenomena. Surface track studies have been performed on various organic and inorganic materials bombarded by atomic as well as cluster ions [141-143]. The application of complementary SFM modes, such as lateral force microscopy, phase imaging or force modulation, has provided additional information about the local variations of certain material properties (*e.g.* adhesion, composition or elasticity) on irradiated surfaces [144].

However, a better understanding of electronic sputtering could be achieved by performing more experiments on well-characterized surfaces. The influence of the target structure could be illuminated further by employing a variety of targets possessing different degrees of binding anisotropy. Also more details should be established on the state of the ejected material. The temporal aspects of sputtering limit the direct comparison between the experimental data and the theoretical models. Future attempts at modeling cluster ejection should involve the consideration of long-term processes, like energy dissipation by ejection, and anisotropic energy diffusion in various solids. The application of the newly available nanotube tips (with tip end radius of ~ 3.5 nm [145]), would probably give much better indication of the crater volumes but may also give rise to additional challenges. *In-situ* analyses of the bombarded surfaces in an ultra-high-vacuum SFM could avoid the condensation of water vapor and other contaminants on the sputtered surface.

Numerous interesting aspects of the NP-film formation can still be studied. For instance, it would be both interesting and useful to measure how the agglomeration process is affected by the flux of the incoming gas-phase nanoparticles and the thickness of the deposit. Unique experiments could be performed by selecting nanoparticle-agglomerates as primary particles for the film deposition. Thermal stability, porosity, fractal dimensions of the agglomerates of these kinds of deposits - as a function of deposition conditions - are challenging problems to explore for basic and applied research as well.

Acknowledgements

References

1. Anonymous, *"Special issue featuring papers from the 8th foresight conference on molecular nanotechnology"*, Nanotechnology **12** (2001).
2. Anonymous, *"Functionalized surfaces and nanostructures for nanotechnological applications"*, Nanotechnology **14** (2003).
3. Appell D, *"Nanotechnology: Wired for success"*, Nature **419**, 553 (2002).
4. Tans SJ, Verschueren ARM, and Dekker C, *"Room-temperature transistor based on a single carbon nanotube"*, Nature **393**, 49 (1998).
5. Grundmann M, Heinrichsdorff F, Ledentsov NN*, et al.*, *"Progress in quantum dot lasers: 1100 nm, 1300 nm, and high power applications"*, Jpn. J. Appl. Phys. **39**, 2341 (2000).
6. Somorjai GA and Borodko YG, *"Research in nanosciences - Great opportunity for catalysis science"*, Catalysis Lett. **76**, 1 (2001).
7. Mal NK, Fujiwara M, and Tanaka Y, *"Photocontrolled reversible release of guest molecules from coumarin-modified mesoporous silica"*, Nature **421**, 350 (2003).
8. Taneike M, Abe F, and S. K, *"Creep-strengthening of steel at high temperatures using nano-sized carbonitride dispersions"*, Nature **424**, 294 (2003).
9. Gleiter H, *"Nanostructured materials: Basic concepts and microstructure"*, Acta Mater. **48**, 1 (2000).
10. Ball P, *"Natural strategies for the molecular engineer"*, Nanotechnology **13**, R15 (2002).
11. Xia Y, Rogers JA, Paul KE*, et al.*, *"Unconventional methods for fabricating and patterning nanostructures"*, Chem. Rev. **99**, 1823 (1999).
12. Spohr R, *Ion tracks and microtechnology* (Friedr. Vieweg & Sohn Verlagsgsellschaft mbH, Braunschweig, 1990).
13. Li J, Stein D, McMullan C*, et al.*, *"Ion-beam sculpting at nanometre length scales"*, Nature **412**, 166 (2001).
14. Thornell G, Spohr R, van Veldhuizen EJ*, et al.*, *"Micromachining by ion track lithography"*, Sensors and actuators A **73**, 176 (1999).
15. Hjort K, Thornell G, Schweitz JA*, et al.*, *"Quartz micromachining by lithographic control of ion track etching"*, Appl. Phys. Lett. **69**, 3435 (1996).

16. Quist AP, Petersson A, Reimann CT*, et al.*, *"Site-selective molecular adsorption at nanometer-scale MeV-atomic-ion-induced surface defects"*, J. of Colloid and Interface Science **189**, 184 (1997).

17. Solis JL, Hoel A, Kish LB*, et al.*, *"Gas-sensing properties of nanocrystalline WO3 films made by advanced reactive gas deposition"*, J. Am. Ceram. Soc. **84**, 1504 (2001).

18. Lee DS, Han SD, Huh JS*, et al.*, *"Nitrogen oxides-sensing characteristics of WO3-based nanocrystalline thick film gas sensor"*, Sensors and actuators B **60**, 57 (1999).

19. Keller V, Bernhardt P, and G. F, *"Photocatalytic oxidation of butyl acetate in vapor phase on TiO2, Pt/TiO2 and WO3/TiO2 catalysts"*, Journal of Catalysis **215**, 129 (2003).

20. Di Paola A, Palmisano L, Venezia AM*, et al.*, *"Coupled semiconductor systems for photocatalysis. Preparation and characterization of polycrystalline mixed WO3/WS2 powders"*, J. Phys. Chem. B **103**, 8236 (1999).

21. Bamwenda GR, Uesigi T, Abe Y*, et al.*, *"The photocatalytic oxidation of water to O-2 over pure CeO2, WO3, and TiO2 using Fe3+ and Ce4+ as electron acceptors"*, Appl. Catalysis A-General **205**, 117 (2001).

22. Granqvist CG, *Handbook of Inorganic Electrochromic Materials* (Elsevier, Amsterdam, 1995).

23. Azens A and Granqvist CG, *"Electrochromic smart windows: energy efficiency and device aspects"*, J. of Solid State Electrochem. **7**, 64 (2003).

24. Bonnell D, *Scanning Probe Microscopy and Spectroscopy: Theory, Techniques and Applications* (John Wiley & Sons Inc., New York, 2001).

25. Quate CF, *"Scanning probes as the gateway to nanotechnology"*, Jap. J. of Appl. Phys., Part 1 **42**, 4777 (2003).

26. Sundqvist BUR, *"Ion track structure probed by plasma desorption mass spectrometry"*, Int. J. Mass Spect. Ion Proc. **126**, 1 (1993).

27. Ferain E and Legras R, *"Track-etch templates designed for micro- and nanofabrication"*, Nucl. Inst. Meth. Phys. Res. B **208**, 115 (2003).

28. Lindeberg M and Hjort K, *"Interconnected nanowire clusters in polyimide for flexible circuits and magnetic sensing applications"*, Sensors and actuators A **105**, 150 (2003).

29. Fleischer RL, Price B, and Walker RM, *Nuclear Tracks in Solids. Principles and Applications* (Univ. of California Press, Berkeley, 1975).

30. Katz R and Kobetich EJ, *"Formation of etchadle tracks in dielectrics"*, Phys. Rev. B **170**, 401 (1968).

31. Trautmann C, Bruchle W, Spohr R*, et al.*, *"Pore geometry of etched ion tracks in polyimide"*, Nucl. Inst. Meth. Phys. Res. B **111**, 70 (1996).

32. Apel P, *"Swift ion effects in polymers: industrial applications"*, Nucl. Inst. Meth. Phys. Res. B **208**, 11 (2003).

51

33. Siwy Z, Dobrev D, and Neumann R, *"Electro-responsive asymmetric nanopores in polyimide with stable ion-current signal"*, Appl. Phys. A **76**, 781 (2003).
34. Maenhaut W, *"Applications of ion-beam analysis in biology and medicine-a review"*, Nucl. Inst. Meth. Phys. Res. B **35**, 388 (1988).
35. Scholz M and Kraft G, *"Calculation of heavy ion inactivation probabilities based on track structure, X-ray sensitivity and target size"*, Rad. Prot. Dos. **52**, 29 (1994).
36. Kaplan M, Forest SR, Schmidt PH*, et al.*, *"Optical and electrical properties of ion-beam-irradiated films of organic molecular solids and polymers"*, J. Appl. Phys. **55**, 732 (1984).
37. Venkatesan T, Compagnini G, and Fotu G, *Ion beam effects in organic molecular solids and polymers* (Elsevier, Amsterdam, 1987).
38. Papaléo RM, Araújo MA, and Livi RP, *"Study of the ion beam induced amorphisation, bond braking and optical gap change processes in PET"*, Nucl. Inst. Meth. Phys. Res. B **65**, 442 (1992).
39. Trautmann C, Schwartz K, and Steckenreiter T, *"Specificity of ion induced damage"*, Nucl. Inst. Meth. Phys. Res. B **156**, 162 (1999).
40. Huczko A, *"Template-based synthesis of nanomaterials"*, Appl. Phys. A **70**, 365 (2000).
41. Thomson JJ, *"Rays of positive electricity"*, Phil. Mag. **20**, 752 (1910).
42. Torgerson DF, Skowronski RP, and Macfarlane RD, Biochem. Biophys. Res. Commun. **60**, 616 (1974).
43. Sundqvist BUR and Macfarlane RD, *252Cf-plasma desorption mass spectrometry* (John Wiley & Sons, New York, 1985).
44. Johnson RE, *"Mechanisms for the desorption of large organic molecules. Part 2"*, Int. J. Mass Spectrom. Ion Process **126**, 17 (1993).
45. Johnson RE, *"Mechanisms for the desorption of large organic molecules"*, Int. J. Mass Spectrom. Ion Process **78**, 357 (1987).
46. Reimann CT, *"Theoretical Models for Sputtering and Desorption of Bio-Organic Molecules under Collisional and Electronic Excitation by Ion Impact"*, Det Kgl. Danske Videnskab. Selskab Mat. Fys. Medd. **43**, 351 (1993).
47. Brinkmalm G, Håkansson P, Kjellberg J*, et al.*, *"DIPLOMA - An experimental system to study MeV and keV particle-induced and photon-induced desorption of molecules"*, Journal of Vacuum Science and Tech. **Sept-Oct**, 2547 (1995).
48. Moshammer R, Matthäus R, Wien K*, et al.*, *Energy and angular distributions of secondary ions ejected from organic solids by MeV ions* (John Wiley & Sons Ltd., 1990).
49. Ens W, Sundqvist BUR, Håkansson P*, et al.*, *"Directional correlation between the primary particle abd ejected molecular ions in electronic sputtering of large organic molecules"*, Phys. Rev. B **39**, 763 (1989).

50. Fenyö D, Hedin A, Håkansson P*, et al.*, *"Radial velocity distributions of secondary ions ejected in electronic sputtering of organic solids"*, Int. J. Mass Spectrom. Ion Process **100**, 63 (1990).

51. Papaléo RM, Demirev P, Eriksson J*, et al.*, *"Measurement of MeV ion track structure in an organic solid"*, Phys. Rev. Lett. **77**, 667 (1996).

52. Håkansson P, *"Desorption Experiments on Organic Insulators with High Energy Particle Beams"*, Det Kgl. Danske Videnskab. Selskab Mat. Fys. Medd. **43** (1993).

53. Betz G and Wien K, *"Energy and angular-distributions of sputtered particles"*, Int. J. Mass Spectrom. Ion Process **140**, 1 (1994).

54. Salehpour M, Håkansson P, Sundqvist BUR*, et al.*, *"Total molecular yields for fast heavy ion induced desorption of biomolecules"*, Nucl. Inst. Meth. Phys. Res. B **13**, 278 (1986).

55. Nafis S, Tang ZX, Dale B*, et al.*, *"Magnetic studies of fine iron and iron-oxide particles"*, J. Appl. Phys. **64**, 5835 (1988).

56. Berkowitz AE, Mitchell JR, Carey MJ*, et al.*, *"Giant magnetoresistance in heterogeneous Cu-Co alloys"*, Phys. Rev. Lett. **68**, 3745 (1992).

57. Edelstein AS, Murday JS, and Rath BB, *"Challenges in nanomaterials design"*, Progress in Materials Science **42**, 5 (1997).

58. Brinker CJ and Scherer GW, *Sol-Gel Science* (Academic Press, Boston, 1990).

59. Eckert J, Holzer JC, Krill CE*, et al.*, *"Structural and thermodynamic properties of nanocrystalline fcc metals prepared by mechanical attrition"*, J. Mater. Res. **7**, 1751 (1992).

60. Hahn H, *"Gas phase synthesis of nanocrystalline materials"*, Nanostr. Mater. **9**, 3 (1997).

61. Hayashi C, Uyeda R, and Tasaki A, *Ultra-Fine Particles: Exploratory Science and Technology*, Noyes, Westwood, 1997).

62. Binnig G, Rohrer H, Gerber Ch*, et al.*, *"Surface studies by scanning tunneling microscopy"*, Phys. Rev. Lett. **49**, 57 (1982).

63. Binnig G, Quate CF, and Gerber Ch, *"Atomic Force Microscope"*, Phys. Rev. Lett. **56**, 930 (1986).

64. Lillehei PT and Bottomley LA, *"Scanning Probe Microscopy"*, Anal. Chem. **72**, 189 (2000).

65. Poggi MA, Bottomley LA, and L. PT, *"Scanning probe microscopy"*, Anal. Chem. **74**, 2851 (2002).

66. Ecke S, Raiteri R, Bonaccurso E*, et al.*, *"Measuring normal and friction forces acting on individual fine particles"*, Review of Scientific Instruments **72**, 4164 (2001).

67. Hamers RJ, *"Scanned probe microscopies in chemistry"*, J. Phys. Chem.-US **100**, 13103 (1996).

68. Garcia R and Perez R, *"Dynamic AFM methods"*, Surface Science Reports **47**, 197 (2002).

69. Hansma HG, Kim KJ, Laney DE*, et al.*, *"Properties of biomolecules measured from atomic force microscope images: A review"*, J. Struct. Biol. **119**, 99 (1997).

70. Henderson E, *"Imaging of living cells by atomic-force microscopy"*, Prog. Surf. Sci. **46**, 39 (1994).

71. Czajka R, Jurczyszyn L, and Rafii-Tabar H, *"Surface physics at the nano-scale via scanning probe microscopy and molecular dynamics simulations"*, Progress in Surface Science **59**, 13 (1998).

72. Davis ZJ, Abadal G, Hansen O*, et al.*, *"AFM lithography of aluminium for fabrication of nanomechanical systems"*, Ultramicroscopy **97**, 467 (2003).

73. Matsuzaki Y, Ota N, Yamada A*, et al.*, *"Formation of nano-oxide regions in p(2+)-GaAs epilayers by localized atomic force microscope probe oxidation for fabrication of nano-structure devices"*, Journal of Crystal Growth **251**, 276 (2003).

74. Gimzewski JK and Joachim C, *"Nanoscale Science of Single Molecules Using Local Probes"*, Science **283**, 1683 (1999).

75. Nakanishi T, Okamoto H, Nagai Y*, et al.*, *"Synthesis and atomic force microscopy observations of the single-peptide nanotubes and their micro-order assemblies"*, Phys. Rev. B **66** (2002).

76. Bohr N, *"On the Theory of the Decrease of the Velocity of Moving Electrified Particles on Passing through Matter"*, Phil. Mag. **25**, 10 (1913).

77. Lindhard J, *"The Barkas effect - or Z13, Z14 - corrections to Stopping of Swift Charged Particles"*, Nucl. Inst. Meth. Phys. Res. B **132**, 1 (1976).

78. Brandt W and Ritchie RH, *Physical Mechanisms in Radiation Biology* (USEC Technical Inf. Centre, Oak Ridge, Tennessee, 1974).

79. Magee JL and Chatterjee A, *Track reactions of radiation chemistry" In Kinetics of Nonhomogenous Processes* (John Wiley&Sons, New York, 1987).

80. Sigmund P, *"Theory of sputtering. I. Sputtering yield of amorphous and polycrystalline targets"*, Phys. Rev. B **184**, 383 (1969).

81. Johnson RE and Sundqvist BUR, *"Electronic sputtering: from atomic physics to continuum mechanics"*, Phys. Today **March**, 28 (1992).

82. Wien K, *"Fast heavy ion induced desorption of insulators"*, Nucl. Inst. Meth. Phys. Res. B **65**, 149 (1992).

83. Fleischer RL, Price PB, and Walker RM, *"Ion explosion mechanism for formation of charged-particle tracks in solids"*, J. Appl. Phys. **36**, 3645 (1965).

84. Dunlop A, Dammak H, and Lesueur D, *"Track formation in metals by electronic processes using atomic and cluster ions"*, Nucl. Inst. Meth. Phys. Res. B **112**, 23 (1996).

85. Watson CC and Tombrello TA, *"A modified lattice potential model of electronically mediated sputtering"*, Rad. Eff. Def. Sol. **89**, 263 (1985).

86. Williams P and Sundqvist BUR, *"Mechanism of sputtering of large biomolecules by impact of highly ionizing particles"*, Phys. Rev. Lett. **58**, 1031 (1987).

87. Johnson RE, Sundqvist BUR, Hedin A, *et al.*, *"Sputtering by fast ions based on a sum of impulses"*, Phys. Rev. B **40**, 49 (1989).

88. Johnson RE and Evatt R, *"Thermal spikes and sputtering yields"*, Rad. Eff. **52**, 187 (1980).

89. Urbassek M and Sigmund P, *"A note on evaporation from heated spikes"*, Appl. Phys. A **35**, 19 (1984).

90. Lucchese RR, *"Thermal spike model for heavy ion induced desorption from surfaces"*, Journal of Chemical Physics **86**, 443 (1987).

91. Bitensky IS and Parilis ES, *"Shock-wave mechanism for cluster emission and organic molecule desorption under heavy-ion bombardment"*, Nucl. Inst. Meth. Phys. Res. B **21**, 26 (1987).

92. Bitensky IS, Goldenberg AM, and Parilis ES, *"Shock wave mevhanism for biomolecule Desorption under heavy ion bombardment"*, Journal de Physique **50**, C2 (1989).

93. Fenyö D and Johnson RE, *"Computer experiments on molecular ejection from an amorphous solid: comparison to an Analytic Continuum Mechanical Model"*, Phys. Rev. B **46**, 5090 (1992).

94. Urbassek HM, *"Molecular-dynamics simulation of sputtering"*, Nucl. Inst. Meth. Phys. Res. B **122**, 427 (1997).

95. Bitensky IS, Goldenberg AM, and Parilis ES, *Spatial distribution of biomolecules sputtered under fast heavy ion bombardment* (Plenum Press, New York, 1991).

96. NoorBatcha I, Lucchese RR, and Zeiri Y, *"Monte-Carlo simulations of gas-phase collisions in rapid desorption of molecules from surfaces"*, J. Chem. Phys. **86**, 5816 (1987).

97. Fenyö D, Sundqvist BUR, Karlsson BR, *et al.*, *"Molecular dynamics study of electronic sputtering of large organic molecules"*, Phys. Rev. B **42**, 1895 (1990).

98. Ziegler JF and Biersack JP, *TRIM92 code*, (1992).

99. Waligórski MPR, Hamm RN, and Katz R, *"The radial-distribution of dose around the path of a heavy-ion in liquid water"*, Nucl. Tracks and Radiat. Meas. **11**, 309 (1986).

100. Salehpour M, Håkansson P, and Sundqvist BUR, *"Damage cross sections for fast heavy ion induced desorption of biomolecules"*, Nucl. Inst. Meth. Phys. Res. B **2**, 752 (1984).

101. Hedin A, Håkansson P, Salehpour M, *et al.*, *"Fast-ion-induced erosion of Leucine as a function of the electronic stopping power"*, Phys. Rev. B **35**, 7377 (1987).

102. Stuglik Z and Sadlo J, *"Latent tracks generated in microcrystalline alpha-L-Alanine and standar bone powder by CO-59-ion-beams as investigated by EPR-method"*, Rad. Meas. **25**, 95 (1995).

103. Papaléo RM, *"Surface tracks on polymers: A means to probe material properties at the nanometer scale?"* Nucl. Inst. Meth. Phys. Res. B **191**, 669 (2002).

104. Kang DJ, Peng NH, Webb R, *et al.*, *"Irradiation damage technology for manufacturable Josephson junctions"*, Nucl. Inst. Meth. Phys. Res. B **188**, 183 (2002).

105. Israelachvili J, *Intermolecular & Surface Forces* (Academic Press Inc., San Diego, CA 92101, 1991).

106. Burnham NA and K. AJ, *Surface Forces and Adhesion* (CRC Press, Boca Raton, FL, 1997).

107. Quate CF, *"The AFM as a tool for surface imaging"*, Surf. Sci. **299-300**, 980 (1994).

108. Mate CM, McClelland GM, Erlandsson R, *et al.*, *"Atomic-scale friction of a tungsten tip on a graphite surface"*, Phys. Rev. Lett. **59**, 1942 (1987).

109. Burnham NA, Colton RJ, and Pollock HM, *"Interpretation of force curves in force microscopy"*, Nanotechnology **4**, 64 (1993).

110. Zhong Q, Innis D, Kjoller K, *et al.*, *"Fractured polymer/silica fiber surface studied by tapping mode atomic force microscopy"*, Surf, Sci. Lett. **290**, L688 (1993).

111. Winkler RG, Spatz JP, Sheiko S, *et al.*, *"Imaging material properties by resonant tapping-force microscopy"*, Phys. Rev. B **54**, 8908 (1996).

112. Burnham NA, Behrend OP, Oulevey F, *et al.*, *"How does a tip tap?"* Nanotechnology **8**, 67 (1997).

113. Kolesnikov DA, Reimann CT, and Vorobyova IV, *"Surface defect formation on gypsum surfaces due to grazing incidence 78.2 MeV I-127 ions: A comparative study employing tapping-mode scanning force microscopy and shadow-replica electron microscopy"*, Nucl. Inst. Meth. Phys. Res. B **122**, 255 (1997).

114. Herbig J, Reimann CT, Bergqvist M, *et al.*, *"Surface track formation on mica surfaces due to grazing incidence 20.2 MeV C60 ions: a comparative study employing shadow-replica electron microscopy, tapping-mode and phase-imaging scanning force microscopy"*, Nucl. Inst. Meth. Phys. Res. B **149**, 119 (1999).

115. Manne S, Cleveland JP, Stucky GD, *et al.*, *"Lattice resolution and solution kinetics on surfaces of amino acid crystals: an atomic force microscopy study"*, J. Cryst. Growth **130**, 333 (1993).

116. Blodgett KB, *"Films buit by Depositing Monomolecular Layers on a solid surface"*, Am. Chem. Soc. **57**, 1007 (1935).

117. Bruninx E and Rudstam G, *"Electro-spraying: a method of making samples for b counting allowing correction for self-scattering and self-absorption"*, Nucl. Inst. Meth. Phys. Res. B **13**, 131 (1961).

118. Säve G, Håkansson P, and Sundqvist BUR, *"Spin deposited submicrometer films of organic molecules for secondary ion mass spectrometry studies"*, Anal. Chem. **59**, 2059 (1987).

119. Ziegler JF, Biersack JP, and Littmark U, *The Stopping and Range of Ions in Solids* (Pergamon Press, New York, 1985).

120. Benninghoven A, Jaspers D, and Sichtermann W, *"Secondary-ion emission of amino acids"*, Appl. Phys. A **11**, 35 (1976).

121. Quist AP, Huth-Fehre T, and Sundqvist BUR, *"Total yield measurements in matrix-assisted laser desorption using a quartz crystal microbalance"*, Rapid Commun. Mass Spectrom. **8**, 149 (1994).

122. Qui Y, Griffith JE, and Tombrello TA, *"A New Technique for Measuring Sputtering Yields at High energies"*, Nucl. Inst. Meth. Phys. Res. B **1**, 118 (1982).

123. Spackman DH, Stein WH, and Moore S, *"Automatic Recording Apparatus for Use in the Chromatography of Amino Acids"*, Anal. Chem. **30**, 1190 (1958).

124. Vorobyova IV and Ter-Ovanes'yan, *"Formation of tracks of heavy multiply charged ions on clean and gold-island-populated surfaces of an insulator"*, Sov. Phys. Solid State **34**, 222 (1992).

125. Thibaudau F, Cousty J, Balanzat E*, et al.*, *"Atomic-force-microscopy observations of tracks induced by swift Kr ions in mica"*, Phys. Rev. Lett. **67**, 1582 (1991).

126. Ackermann J, Angert N, Neumann R*, et al.*, *"Ion track diameters in mica studied with scanning force microscopy"*, Nucl. Inst. Meth. Phys. Res. B **107**, 181 (1996).

127. Neumann R, Ackermann J, Anger N*, et al.*, *"Ion tracks in mica studied with scanning force microscopy using force modulation"*, Nucl. Inst. Meth. Phys. Res. B **116**, 492 (1996).

128. Daya DDNB, Hallen A, Eriksson J*, et al.*, *"Radiation damage features on mica and L-valine probed by scanning force microscopy"*, Nucl. Inst. Meth. Phys. Res. B **106**, 38 (1995).

129. Reimann CT, *"Some comments on pressure-pulse/shock-wave desorption in a real material"*, Nucl. Inst. Meth. Phys. Res. B **95**, 181 (1994).

130. Hedin A, Håkansson P, Sundqvist BUR*, et al.*, *"Ion -track model for fast ion-induced desorption of molecules"*, Phys. Rev. B **31**, 1780 (1985).

131. Ramos SMM, Bonardi N, Canut B*, et al.*, *"Damage creation in alpha-Al2O3 by MeV fullerene impacts"*, Nucl. Inst. Meth. Phys. Res. B **143**, 319 (1998).

132. Brunelle A, DellaNegra S, Deprun C*, et al.*, *"High desorption-ionization yields of large biomolecules induced by fast C-60 projectiles"*, Int. J. of Mass Spectr. and Ion Proc. **164**, 193 (1997).

133. Säve G, Håkansson P, Sundqvist BUR*, et al.*, *"Crater formation in Langmuir-Blodgett-films induced by electronic sputtering with fast heavy-ions"*, Appl. Phys. Lett. **51**, 1379 (1987).

134. Schmidt R, Schoppmann Ch, Brandl D*, et al.*, *"Heavy-ion-induced desorption of organic-molecules studied with Langmuir-Blodgett multilayer systems"*, Phys. Rev. B **44**, 560 (1991).

135. Sundqvist BUR, *Sputtering by particle bombardment* (Springler, Berlin, 1991).

136. Vorobyova IV, *"Processes on the surface and subsurface layer of solids in heavy multicharged ion tracks formation"*, Rad. Meas. **25**, 131 (1985).

137. Baranov I, Bogdanov S, Novikov A*, et al.*, *"Electronic sputtering of nanometric cluster ions of gold from ultradispersed targets of gold by fission fragments; Masses and energies of cluster ions"*, Nucl. Inst. Meth. Phys. Res. B **122**, 329 (1997).

138. Soderlund J, Kiss LB, Niklasson GA*, et al.*, *"Lognormal size distributions in particle growth processes without coagulation"*, Phys. Rev. Lett. **80**, 2386 (1998).

139. Maugis D, *"Adhesion of spheres- the JKR-DMT transition using Dugdale model"*, J. Colloid and Interf. Sci. **150**, 243 (1992).

140. Eriksson J, Demirev P, Håkansson P*, et al.*, *"Total yield and polar angle distributions of biomolecules sputtered by fast heavy ions"*, Phys. Rev. B **54**, 15025 (1996).

141. Schwartz K, Trautmann C, and Neumann R, *"Electronic excitations and heavy-ion-induced processes in ionic crystals"*, Nucl. Inst. Meth. Phys. Res. B **209**, 73 (2003).

142. Daya DDNB, Reimann CT, Håkansson P*, et al.*, *"Crater formation due to grazing incidence C-60 cluster ion impacts on mica: A tapping-mode scanning force microscopy study"*, Nucl. Inst. Meth. Phys. Res. B **124**, 484 (1997).

143. Brunelle A, DellaNegra S, Deprun C*, et al.*, *"High desorption-ionization yields of large biomolecules induced by fast C-60 projectiles"*, Int. J. Mass Spect. Ion Proc **164**, 193 (1997).

144. Neumann R, *"Scanning probe microscopy of ion-irradiated materials"*, Nucl. Inst. Meth. Phys. Res. B **151**, 42 (1999).

145. Dai H, Hafner JH, Colbert DT*, et al.*, *"Nanotubes in scanning probe microscopy"*, Nature **384**, 147 (1996).

Acta Universitatis Upsaliensis

Comprehensive Summaries of Uppsala Dissertations
from the Faculty of Science and Technology

Editor: The Dean of the Faculty of Science and Technology